Hydraulic transport through calcite bearing faults with customized roughness: Effects of normal and shear loading.

M. Acosta[1*], R. Maye[1#], M. Violay[1]

[1]EPFL, LEMR, Lausanne, Switzerland.

[#] now at: KFSA, Lausanne, Switzerland.

*Corresponding author: Mateo Acosta (mateo.acosta@epfl.ch)

Key Points:

- Marble fractures with customized roughness are used to study how roughness parameters affect fluid flow under upper crustal conditions
- Fracture transmissivity under normal stress shows a non-monotonic dependence with RMS roughness and macroscopic wavelength.
- Reversible shear loading doesn't change transmissivity. Irreversible displacement correlates with fracture geometry at low normal stress.

Abstract

Understanding fluid flow in rough fractures is of high importance to large scale geologic processes and to most anthropogenic geo-energy activities. Here, we conducted fluid transport experiments on Carrara marble fractures with a novel customized surface topography. Transmissivity measurements were conducted under mechanical loading conditions representative of deep geothermal reservoirs (normal stresses from 20 to 70 MPa and shear stresses from 0 to 30 MPa). A numerical procedure simulating normal contact and fluid flow through fractures with complex geometries was validated towards experiments. Using it, we isolated the effects of roughness parameters on fracture fluid flow. Under normal loading, we find that i) the transmissivity decreases with normal loading and is strongly dependent on fault geometry ii) the standard deviation of heights (RMS) and macroscopic wavelength of the surface asperities control fracture transmissivity. Transmissivity evolution is non-monotonic, with more than 4 orders of magnitude difference for small variations of macroscopic wavelength and RMS roughness. Reversible shear loading has little effect on transmissivity, it can increase or decrease depending on the combined contact geometry and overall stress state on the fault. Finally, irreversible shear displacement (up to 1 mm offset) slightly decreases transmissivity contrary to common thinking. The transmissivity variation with irreversible shear displacements can be predicted geometrically at low normal stress only. Finally, irreversible changes in surface roughness (plasticity and wear) due to shear displacement result in a permanent decrease of transmissivity when decreasing differential stress. We discuss the implications for Enhanced Geothermal Systems stimulation.

1 Introduction

Fluids are pervasive in Earth's crust. They interact with rocks, modifying their physical properties and deformation mechanisms. In turn, host rocks control the way fluids migrate in the crust either due to natural forcing or to anthropogenic activities (Sibson, 1994;1996). Rock masses in the brittle-crust are pervasively fractured and have permeabilities ranging from around 10^{-16} to 10^{-17} m^2 (Townend and Zoback, 2000; Faulkner et al., 2010). These permeability values are more than two to three orders of magnitude larger than those of the intact rock matrix (10^{-21} to 10^{-19} m^2) at depths ranging from ~2 to 15 km. Most of the fluid flow needs therefore to be controlled by single fractures or fracture networks. Thus, it is of outmost importance to

understand how fractures and faults transport fluids in the subsurface. This is particularly valid for the safe, and clean development of underground anthropogenic geo-energy activities such as geothermal energy exploitation (Breede et al., 2013; Violay et al., 2015; 2017). Indeed, a popular strategy for enhancing fluid transport in Enhanced Geothermal Systems (EGS) is fracture hydro-shearing, by fluid injection. It consists on reactivating pre-existing faults to increase the deep crystalline reservoir's permeability (Cladouhos et al., 2010; Breede et al., 2013). Nevertheless, the enhancement of fluid flow following stimulations in such reservoirs remains poorly predicted. A too low subsurface production flow rate results in economic losses while too high flow rates can lead to fluid leak off and reactivation of faults located far from the injection wells. This was the case of the St.Gallen geothermal project (Zbinden et al., 2020) and possibly of several other injection induced seismicity cases (Ellsworth, 2013; Lengliné et al., 2014; Goebel and Brodsky, 2018; Yeck et al., 2016; Kim et al., 2018; Grigoli et al., 2017). The poorly estimated flow rates partly arise due to the difficulties in detecting the fracture networks in the underground and partly due to the difficulties of estimating fluid flow through rough fractures with complex surface topographies, submitted to large stresses. Natural rock fractures show self-similar roughness properties (Brown and Scholz, 1985; Power et al., 1987; Brown, 1987; Candela et al., 2009; 2012; Renard et al., 2013) at all scales. In addition, exhumed fault walls often show grooves parallel to the main slip direction (Petit, 1987; Means, 1987; Power et al., 1987; Power and Tullis, 1989; Engelder and Scholz, 1976; Toy et al., 2017). These features result in surfaces with high elevation zones (peaks) and low elevation zones (or valleys). Several methods exist for quantifying the statistical properties of rough surfaces (Brown and Scholz, 1985; Grasselli and Eger, 2003; Candela et al., 2009; 2012; Renard et al., 2013; Jacobs et al., 2017; Yastrebov et al., 2017). As two fracture surfaces come in contact they form a three-dimensional distribution of local contacts (asperities) and voids (apertures) which in turn determine how fluids can circulate through the fracture.

The geometrical aperture distribution is strongly dependent on the contact geometry and on the stress applied on the fracture because they both affect the equivalent hydraulic aperture, through which fluids can flow (Zimmerman and Bodvarsson, 1996). Complex contact geometries can also lead to flow channeling in fractures (Watanabe et al., 2009; Kang et al., 2016) drastically affecting their hydraulic transport capacity. Most experimental works have been performed either at low stresses (Patir and Cheng, 1978; Witherspoon et al., 1980; Park and Song, 2013;

Tanikawa et al., 2010; Wenning et al., 2019), or on faults with constant roughness (Watanabe et al., 2008; Faoro et al., 2009; Rutter and Mecklenburgh, 2017; 2018).

The application of normal stress has been shown to increase the real contact area between the two fracture walls, and to reduce the geometrical aperture and hydraulic transmissivity (Witherspoon et al., 1980; Walsh, 1981; Renshaw, 1995; Brown 1987; Brown et al., 1998; Pyrak-Nolte and Morris, 2000; Watanabe et al., 2008; 2009; Kang et al., 2016; Rutter and Mecklenburgh, 2017; 2018). After passing a stress value (percolation threshold) the fracture reaches a configuration where further increases in normal stress result in small changes in the hydraulic aperture. Then, fracture transmissivity remains constant due to the formation of preferential channels in between the highly stressed asperities (Brown et al., 1998; Pyrak-Nolte et al., 1988; Durham, 1997; Watanabe et al., 2008; 2009; Kang et al., 2016). The influence of reversible shear loads (in the elastic domain) has been rarely studied experimentally. In some few observations, it is seen that reversible shear loading (elastic loading, with no displacement) can cause a slight decrease in fracture transmissivity (in relatively smooth fractures of hard rock; Faoro et al., 2009; Rutter and Mecklenburgh, 2017; 2018). Most of the effort has been put to determine the effect of irreversible shear displacement on fracture transmissivity, usually considering large displacements (more than 1-20 millimeters) at low stresses (usually lower than 20 MPa), and/or on rock fractures generated by tensile or shear fracturing as well as on artificial rock proxies (Carey et al., 2015; Ishibashi et al., 2012; Lee and Cho, 2002; Yeo et al., 1998; Zambrano et al., 2018; Pyrak-Nolte et al., 1988; Olsson and Brown, 1993; Esaki et al., 1999; Wenning et al., 2019; Chen et al., 2000; Watanabe et al., 2008; 2009). From such studies, the usual knowledge with respect to the influence of shear displacement on transmissivity is that it strongly increases hydraulic transport on the fault. In contrast, recent studies (Rutter and Mecklenburgh, 2017; 2018) have shown that for displacements inferior to 1 mm, on real rock samples with smooth surfaces, at high stresses (up to 100 MPa normal stress) the transmissivity rather decreases or remains fairly constant with increasing shear displacement. These types of studies seem more relevant to fault reactivation due to anthropogenic activities (in EGS stimulation for example) particularly because the reactivation of reservoir faults needs to target small displacements to avoid large magnitude seismicity.

In this work, we developed an experimental technique to customize the roughness of hard-rock fracture surfaces by imposing different macroscopic wavelengths in sub-orthogonal and sub-

parallel directions with respect to the sense of fluid flow. Then, the fluid flow through the wavy-rough fractures was experimentally measured both under normal loading only (up to 40 MPa) and under reversible shear loading (up to shear and normal stresses close to 30 and 80 MPa respectively). The fractures loaded in shear were then submitted to irreversible shear displacement (up to 1 mm total offset). A numerical procedure that first simulates the normal contact between wavy-rough surfaces and then fluid flow through them was developed and verified with the experimental results. It is noteworthy that the numerical procedure consists on a combination of open-source models. Through the use of the calibrated numerical procedure, we isolated the effects of roughness parameters on fracture transmissivity under normal load. The numerical procedure was also used to isolate the influence of reversible shear loads on transmissivity. Finally, we evaluated how the small transmissivity changes during irreversible shear displacement can be predicted by a change in geometry of the fracture surface for different applied normal stresses.

2. Experimental materials and methods.

2.1 Starting samples with customized roughness.

The samples were 75 mm long cylinders (36 mm diameter) of Carrara marble. Carrara marble has a well characterized mineralogy (~99 vol% calcite), low porosity (~1%), fine grain (average grain size <0.5 mm), and high homogeneity and isotropy (Chen, 1995; Pieri et al., 2001; Delle-Piane et al., 2015). Its mechanical properties (Young's modulus ~30 GPa and uniaxial compressive strength ~160 GPa; Edmond and Paterson 1972; Paterson and Wong, 2005) make it a standard in rock mechanics and an ideal material for laboratory testing. For normal loading experiments, two semi-cylinder's vertical flat faces were ground prior to sample coring, to obtain a perfect semi-circular geometry. For shear loading and reactivation experiments, the cylinders were cored first, and then saw-cut at 30° towards the cylinder's long axis to create an oriented fracture. The fracture's faces were ground flat to ensure perfect contact. Finally, an injection/extraction borehole of $2\ mm$ diameter was drilled in each half sample from the horizontal flat surface (in contact with the top/bottom anvils) to inject/extract fluid directly into/from the fracture. In saw cut configuration, the resulting fracture was of elliptical shape with long axis $2a_e = 72\ mm$ and short axis $2b_e = 36\ mm$. The elliptical contacting fracture surfaces

had a nominal area $A{\sim}2036\ mm^2$. Prior to loading, the distance between boreholes centers was of $60\ mm$.

For all experiments, a customized fracture roughness was imposed to each flat surface of the half-samples using a vertical-axis milling machine. The machine (Figure 1e) is composed of three main elements: i) A table where the half samples were locked and leveled to a horizontal position. ii) A rotary milling cutter mechanically linked to a rotating spindle whose spin is controlled by a motor. The rotary cutter can be lowered to enter in slight contact with the half sample iii) An automatically advancing arm mechanically fixed to the rotary cutting tool. As the rotary cutting tool advances, it periodically removes rock material over the tool blade's edge, making arc shaped grooves on the sample's surface. The grooves' wavelengths are smaller for faster advancement speeds and larger for slower ones, resulting in customized roughness depending on the advancement speeds.

The different experimental geometries are detailed in Table 1 and shown in Figure 1a-d. In the sample's names, the first subscript denotes large or small macroscopic wavelength (L or S) and the second subscript denotes the sense of fluid flow with respect to the macroscopic grooves (P for sub-parallel and O for sub-orthogonal). Finally M_f denotes the sample with no imposed macroscopic wavelength where the roughness was manually imposed through #80 grit. In all experiments, fluid flow occurred following the y-axis (fracture's long axis) as defined in Figure 1. In experiments with shear loading and displacement, shear occurred along the y-axis.

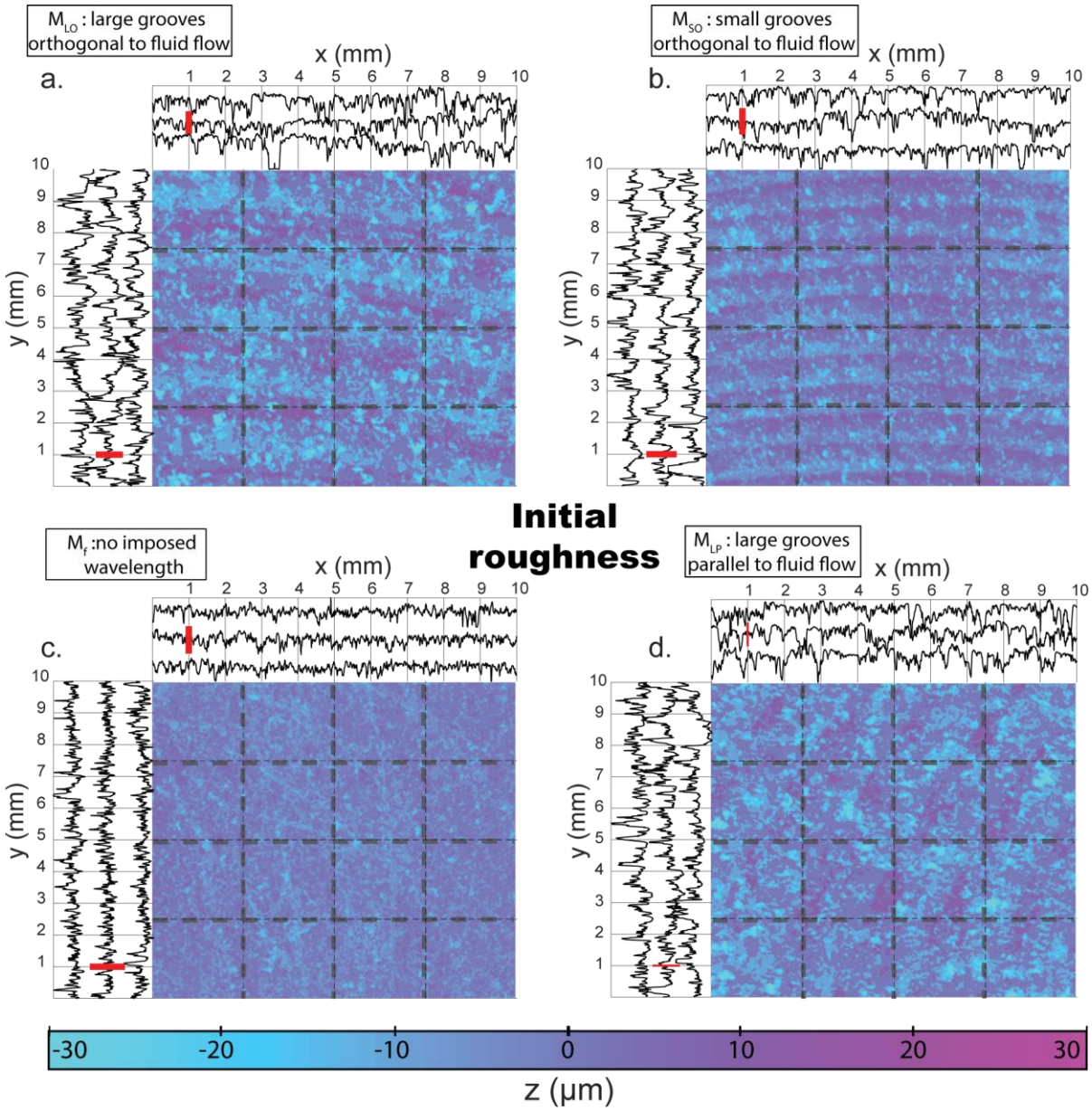
M_LO : large grooves orthogonal to fluid flow
a.
x (mm)
y (mm)
M_SO : small grooves orthogonal to fluid flow
b.
Initial roughness
M_f :no imposed wavelength
c.
M_LP : large grooves parallel to fluid flow
d.
-30
-20
-10
0
10
20
30
z (μm)

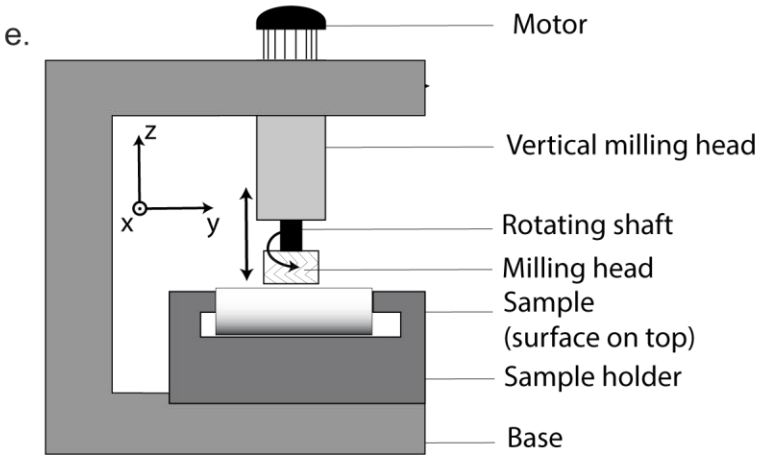
e.
Motor
Vertical milling head
Rotating shaft
Milling head
Sample
(surface on top)
Sample holder
Base
z
x
y

Figure 1: Customized initial fracture roughness. a-d. Roughness measurements of the four types of experimental samples. Colorbar represents the measured heights over the area. The transects in x-axis and y-axis in dotted lines are presented in the top and left plots respectively. For reference, a red bar represents 30 micrometers height. a. Sample M_{LO}, large wavelength with grooves sub-orthogonal to fluid flow and shear direction. b. Sample M_{SO}, small wavelength with grooves sub-orthogonal to fluid flow and shear direction. c. Sample M_f, no imposed macroscopic wavelength. d. Sample M_{LP}, large wavelength with grooves 'sub-parallel' to fluid flow and shear direction. d. Diagram of the milling apparatus. Displacement rate over the y-axis can be controlled. The x-axis is fixed. Movement over the z-axis can be changed and fixed at a given position (0.1 mm under the sample's surface).

2.2 Roughness measurement and data processing.

The measurement of surface roughness was performed using a 3D optical profilometer (Contour GT-I 3D Optical Microscope by Bruker Nano surfaces Division). The tool uses green light interferometry to determine the surface topography of the sample with an accuracy down to ~100 nm. The green light pulse has an area of ~1 mm^2. A motorized base allows sample movement in the x and y directions (minor and major axis of the fracture respectively). The tool allows automatic scanning of large surfaces by performing several measurements with a given overlap (here of 20%) which are later stitched together to reconstruct a larger surface topography. Under this configuration, two overlapping areas of sample M_{LO} were analyzed. The first area had a surface of 1 cm*1 cm and the second area had a 3 cm * 3 cm area. The measurement results showed that the surfaces' statistical properties (radially averaged 2-Dimensional PSD) are transitionally invariant. Hence, it is assumed that taking only a portion of 1 cm^2 of the sample's surface instead of taking the whole area gives statistically the same result. Thus, for time purposes, only an area of 1 cm^2 was analyzed on the profilometer for all other samples.
The following corrections were then applied to the measured data (x,y,z profiles): i) Tilt removal. The intrinsic tilt due to levelling error at measurement was removed. ii) Interpolation of missing points. Missing values are a specific consequence of rough surface because the reflected light path can be cut when large slopes are encountered (Jacobs et al., 2017). A 2D nearest

neighbor interpolation technique (Pingel et al., 2013) was used in order to interpolate the missing data points. iii) Correction for sampling artifacts. The sampling theorem states that the minimum wavenumber to be considered in spectral analysis should be smaller than the Nyquist frequency $f_N = \frac{N}{2L}$ where N is the total number of points in the sampled domain (N= 5044) and L=10 mm is the length of the measured domain. Thus, the cut-off wavector (e.g the maximum wavevector analysed) should be $q_{cut} = 2.5e5\ m^{-1}$. A low-pass Gaussian filter was applied to remove all wavevectors higher than q_{cut} in the data. Finally, to evaluate the properties of rough surfaces (Figure 7). a radially averaged 2D Power Spectral Density analysis with radially symmetric Welch windows was performed to avoid artifacts (PSD, Jacobs et al., 2017; Kanafi, 2019).
It is important to notice that in the rest of the manuscript the roughness parameters are evaluated with the available data. For example, the Hurst exponent is evaluated on windows smaller than one order of magnitude thus leading to an intrinsic error related to the availability of the data (more data could be obtained through higher/lower resolution measurements to complement the dataset). Similar difficulties arise on the estimation of the roll-off wavevector for the experimental samples. Notwithstanding the estimated intrinsic errors, the same technique was applied for all the measured samples. Thus, the comparative analysis presented remains robust even though the absolute values of these parameters might not be as accurate as desired.

2.3. Experimental set-ups and flow through experiments.

The experimental set up was an oil-medium tri-axial Hoek-cell (Figure 2) of the Laboratory of Experimental Rock Mechanics (LEMR) at EPFL, Switzerland. The cell can hold 70 MPa (+- 50 kPa resolution) in confinement pressure ($\sigma_3 = \sigma_2$). For flow through experiments, the top and bottom anvils were specifically designed to allow controlled fluid pressures and volumes independently at the top and bottom ends of the samples (Figure 2). The pressure/volume controllers have a capacity of 200 cm^3 (+-1mm^3 resolution) in volume and 30 MPa (+- 10 kPa resolution) in pressure.
One experiment was performed to evaluate the matrix permeability of Carrara marble and have a point of comparison for the fracture fluid flow experiments. Due to the low permeability of the rock matrix, an oscillatory fluid flow method was used under the same experimental set-up. Details of the oscillatory fluid flow method can be found in Bernabé et al. (2006) and Acosta and Violay (2020). Matrix permeabilities ranged from ~5.99 e-19 m^2 at σ_3'=8 MPa to 4.92e-20 m^2 at

215 σ_3'=20 MPa (Figure 2b) and the exponential decay seems consistent with previous literature
216 studies of the permeability of Carrara marble (Chen, 1994; Zhang et al., 2014; Delle-Piane et al.,
217 2015).
218
219

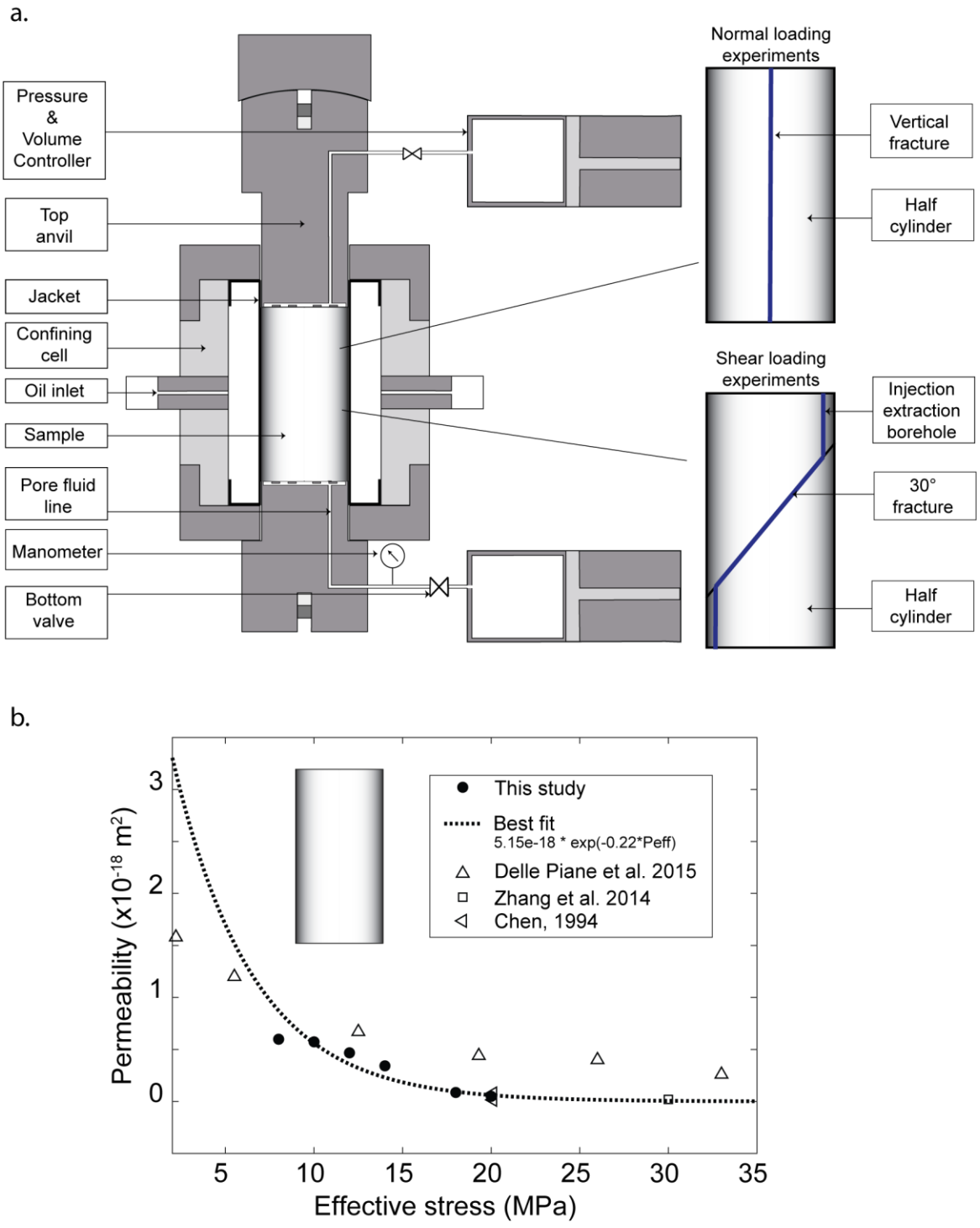

Figure 2. Experimental set-up and flow through experiments. a. The Hoek-cell tri-axial set-up with customized fluid pressure system for flow through experiments (After Noel et al., 2019). Two types of sample geometries were used for different experiment types (under normal and shear loading). b. Permeability of intact Carrara marble cylinder function of effective stress.

Black dots represent the experimentally measured values. Empty symbols represent data from the literature. Dotted line represents the best exponential decay fit to the experimental data produced in this study.

Experiments under normal loading.

The half cylinders were clamped together and let to saturate in a vacuum chamber for a minimum of one-week. Following this, samples were confined to $\sigma_3 = 5$ MPa and fluid pressure (p_f) to 1 MPa during a minimum of 120 minutes for additional (pressurized) saturation. Once fluid and confinement pressures and volumes reached an equilibrium, σ_3 was increased to the target pressure of 43 MPa and p_f was changed stepwise to study the effect of effective normal stress ($\sigma'_N = \sigma'_3 = \sigma_3 - p_f$ = 28,30,32,34,36,38,40 MPa; Figure 3a). At each step, a differential pressure Δp_f = 0.3 MPa was imposed between the top and bottom ends of the sample and the fluid flow rate (Q in $m^3.s^{-1}$) was measured (Figure 3a,b). Because the flow rate on the fracture was more than 3 orders of magnitude larger than in an intact Marble cylinder (Figure 2b), it is reasonable to assume that all the flow occurred through the fracture.

For each σ'_N step, the fluid flow through a fracture was quantified by the product of the permeability (k in m^2) and the effective thickness (t in m) (Rutter and Mecklenburgh; 2017; 2018). kt is called the fracture's hydraulic transmissivity (kt in m^3) which can be estimated directly from Darcy's law as:

$$kt = \frac{\mu.Q}{w.\frac{\Delta P}{L}}$$

with μ the dynamic viscosity of the fluid, w the fracture's width and L its length.

Experiments under shear loading.

The procedure to saturate the samples, place them in the cell, and take them to isostatic loading ($\sigma'_1 = \sigma'_3$) was the same as for normal loading experiments. For the shear experiments, confining pressure σ_3 was either 15 or 35 MPa and p_f was 5 or 15 MPa respectively (so that the effective confinement $\sigma'_3 = 10$ and $20\ MPa$). Then, the axial displacement was increased by steps of 0.1 mm at a displacement rate of 10^{-6} mm.s^{-1} Such a low displacement rate was used to allow fluid pressures equilibrium on the fault during shear loading (i.e fault drainage). Under saw-cut configuration, both shear and normal stresses on the fault increased with increase of axial displacement and were calculated as:

$$\tau = \frac{(\sigma_1' - \sigma_3')}{2}\sin(2\theta)$$

And

$$\sigma'_N = \frac{(\sigma_1' + \sigma_3')}{2} + \frac{(\sigma_1' - \sigma_3')}{2}\cos(2\theta)$$

with θ the angle between the saw-cut and the vertical.

The final axial displacement in our experiments was of ~1.1 or 1.2 mm. As fault reactivation (e.g. departure from elasticity) occurred often slightly after ~0.1 mm displacement, the final shear offset was of ~1 mm in most experiments. At every displacement step, the piston's position was held constant and a differential fluid pressure of 0.3 MPa was imposed between the injection and extraction boreholes to measure sample's transmissivity (Figure 3c,d).

The steady state flow-rate Q was determined and the hydraulic transmissivity was estimated from the flow lines in a perfect elliptical surface using the dipole image method of Rutter and Mecklenburgh (2017; 2018) such that the transmissivity (product of permeability and equivalent hydraulic aperture) writes (Rutter and Mecklenburgh, 2017; 2018; Passelègue et al., 2020; Almakari et al., 2020):

$$kt = \frac{Q.\mu.\log_{10}\left(\frac{2a_e}{r_0} - 1\right)}{B.\pi.\frac{\mathrm{d}P}{dx}}$$

with a_e the half distance between the injector and extractor boreholes; r_0 the borehole diameter; $\frac{dP}{dx}$ the spatial pressure gradient between the boreholes; and B a constant close to unity (Rutter and Mecklenburgh, 2017; Passelègue et al., 2020; and Almakari et al., 2020).

It is noteworthy that here, no corrections for the changes in elliptical surface geometry were made (see Tembe et al., 2010) because the total displacement on the saw/cut was $< 1.2\ mm$, resulting in a change in nominal contact area lower than 8% which would result in less than 0.5% change in transmissivity.

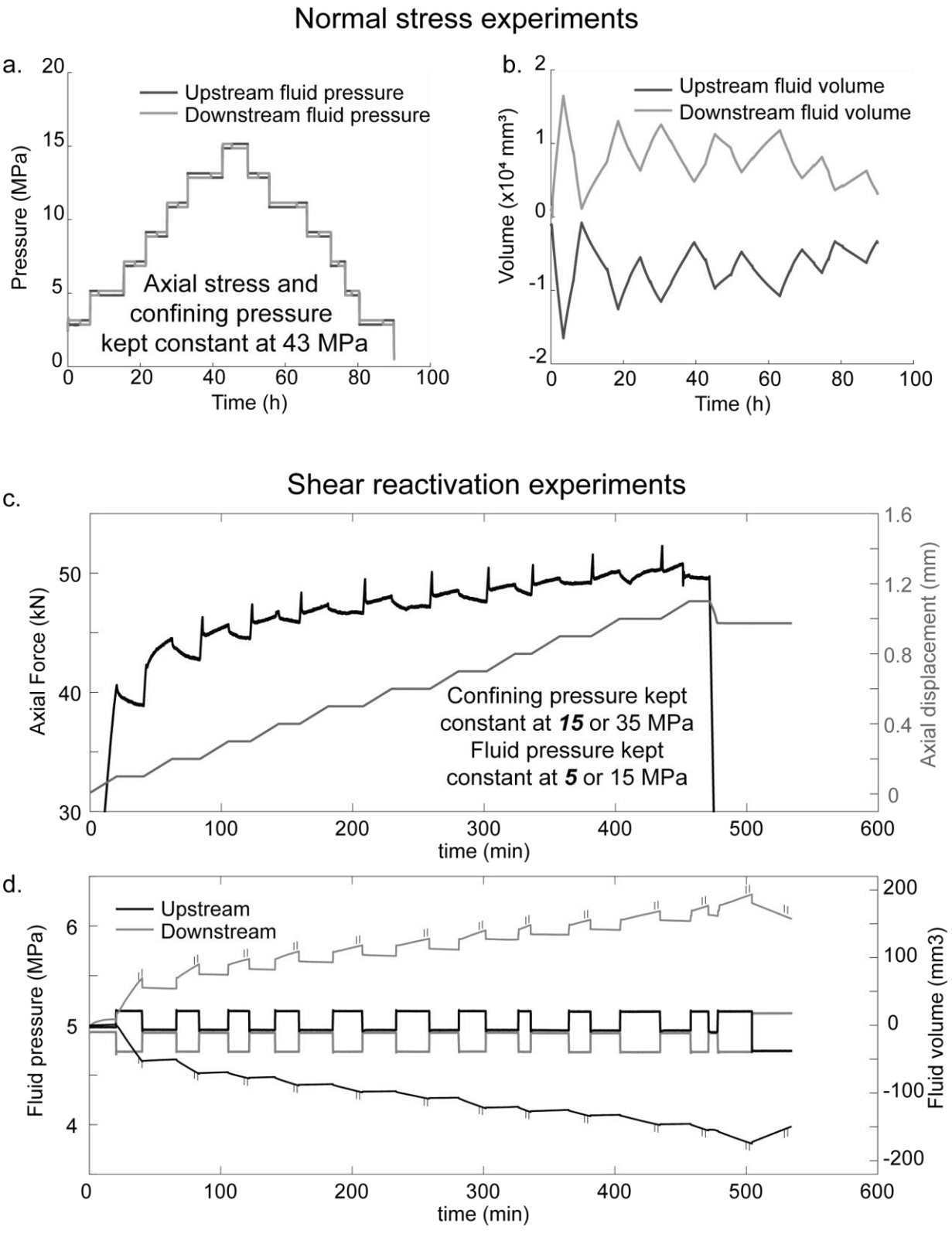

Figure 3. Example experiments. a,b. Normal loading experiments. Axial stress and confining pressure were fixed at 43 MPa. The changes in mean fluid pressure led to a change in effective

normal stress applied on the fracture. a. Upstream and downstream fluid pressures versus time. b. Upstream and downstream volumes versus time. The imposed differential pressure resulted in a symmetric volume rate at the pressure/volume controllers which was held until achieving a steady state. c,d. Shear loading experiments. c. Axial force (black) and axial displacement (grey) versus time. The increase in axial displacement led to a spontaneous evolution of the axial force (therefore of shear and normal stress) applied on the 30° saw-cut fracture. d. Fluid pressures (left x-axis) and volumes (right y-axis) versus time. A differential pressure of 0.3 MPa was imposed at every displacement step to measure transmissivity in steady state. The example in panels c and d is given for an experiment at 10 MPa effective confinement.

Experiment type	Sample name	Grooves[a]	σ_3 MPa	Pf MPa	σ_3' MPa	σ_{Nss}[b] MPa	$err\ \sigma_{Nss}$[c] MPa	τ_{ss}[b] MPa	$err\ \tau_{ss}$[c] MPa	f_{ss}[b] -	d_{ss}[d] mm	$err\ d_{ss}$[e] mm	d_{end}[f] mm
Permeability	Intact	X	23	3:3:15	8:3:20	X	X	X	X	X	X	X	X
Normal loading	M_{LO}	⊥	43	3:2:15	28:2:40	28:2:40	X	X	X	X	X	X	X
Normal loading	M_{SO}	⊥	43	3:2:15	28:2:40	28:2:40	X	X	X	X	X	X	X
Normal loading	M_f	no	43	3:2:15	28:2:40	28:2:40	X	X	X	X	X	X	X
Normal loading	M_{LP}	‖	43	3:2:15	28:2:40	28:2:40	X	X	X	X	X	X	X
Shear loading	M_{LO}	⊥	15	5	10	37.50	2.10	15.78	1.21	0.61	0.17	0.01	1.10
Shear loading	M_{SO}	⊥	15	5	10	34.37	2.40	14.10	1.39	0.58	0.15	0.01	1.10
Shear loading	M_f	no	15	5	10	34.04	1.89	13.89	1.09	0.59	0.15	0.01	1.10
Shear loading	M_{LP}	‖	15	5	10	30.94	3.00	12.36	1.73	0.55	0.29	0.01	1.10
Shear loading	M_{LO}	⊥	35	15	20	66.30	3.60	27.01	2.08	0.58	0.26	0.01	1.17
Shear loading	M_{SO}	⊥	35	15	20	61.43	2.40	23.97	1.39	0.55	0.22	0.01	1.26
Shear loading	M_f	no	35	15	20	58.71	2.25	22.02	1.30	0.54	0.23	0.01	1.09
Shear loading	M_{LP}	‖	35	15	20	59.46	1.62	22.79	0.94	0.54	0.29	0.01	1.12

[a] parallel or orthogonal to fluid flow.
[b] at fault reactivation.
[c] estimated from the difference between maximum and minimum during shear sliding.
[d] initiation of "steady state" sliding.
[e] estimated error in the determination of "steady state" sliding.
[f] final axial displacement reached.

Table 1. Experiments performed and summary of mechanical results.

3 Numerical Methods

3.1. Generation of artificial surfaces.

Artificial wavy-rough surfaces were independently generated through use of the algorithm by M.M. Kanafi (2018). The algorithm uses the roughness parameters (measured with the profilometer) from the power spectral density of surface heights (h_{RMS}, H and q_r) to generate an artificial randomly rough surface with the corresponding properties. In addition to the randomly

generated rough surface, the experimental samples had a customized macroscopic wavelength (see section 2.1) which represents a singularity at a given wavevector in the radially averaged PSD's (Jacobs et al., 2017). The macroscopic wavelength and the corresponding amplitude was evaluated through the profilometer measurements (Table 2). The final surfaces are the resultant of a random roughness created from the artificial surface generator on top of a sinusoidal macroscopic wavelength estimated from the experimental samples (Figure 4a). The total roughness was adjusted so that the h_{RMS} of the sum of the two surfaces is equal to the true h_{RMS} measured on the experimental sample.

3.2. Surface contact under normal stress.

To simulate contact of two opposing surfaces resulting from lithostatic pressure in Geo-energy reservoirs (represented by σ_3' in the experiments), a half-space based, dry contact model from *Tribonet* was used (Lubrecht and Ioannides, 1991; Akchurin et al., 2015; https://www.tribonet.org/cmdownloads/tribology-simulator/). The model uses the artificially generated surfaces discretized to either 2048*682 (for model calibration) or 768*256 nodes (for parametric analysis). Solid material properties were assigned to the contact bodies (which can differ but are here taken equal) described by a saturating elastic stress-strain relationship (e.g. the deformation is purely elastic until a stress threshold is reached, then stress remains constant with increasing strain). The parameters used here are the material's Young's modulus E (here 30.2 GPa) and the Poisson's ratio ν (here 0.3) for elasticity (measured from a Marble deformation experiment shown in Annex 1); and the yield stress σ_y (here 0.2 GPa; Violay et al., 2014) which describes the limit of plasticity (or saturation threshold). The simulated load applied between the half spaces corresponds to the macroscopic normal stress (here σ_3') over the nominal contact area $A_n = L \cdot w$ (see Table 1 and section 2.3). The contact problem is solved under plane-strain and takes into account the mechanical interactions between micro contacts (Polonsky and Keer,1999) by the use of a double-continuum convolution integral. It calculates how the deflection at each mesh node affects the surrounding nodes. The calculation iterates until convergence of the deflection at all nodes (Lubrecht and Ioannides, 1991; Polonsky and Keer., 1999; Akchurin et al., 2015; and *Tribonet*). As outputs, two-dimensional real contact area (A_r) maps and geometrical aperture ($e_m\ (x, y)$) maps were recovered at each studied effective confining pressure (Figure 4b). Note that in the aperture maps, a zero-aperture value is not

allowed in our procedure. Thus, the contacting zones were replaced with apertures more than ten orders of magnitude smaller than the mean aperture to avoid numerical issues for fluid flow calculation.

3.3. Surface contact under shear loading.

It is noticeable that the contact model does not include a shear stress component analysis nor a wear analysis. From our knowledge, integrating an elasto-plastic shear component and wear components to the analysis is not a straightforward task and is out of the scope of this study (Aghababaei et al., 2016; Milanese et al., 2019; Molinari et al., 2018; Frerot et al., 2019).
In order to simulate the effect of shear displacement on fracture transmissivity we simplified the problem to the shift between the two opposing artificial surfaces of a given displacement (Figure 4d). For this model, two artificial rectangular surfaces (32 mm*64 mm; equivalent to the ellipsis area to simplify the problem) were generated with shifts of 0.1 mm in the y-direction and put into contact using the procedure described above. For each sample, a total of 10 surface pairs was computed to evaluate the evolution of transmissivity with increasing displacement up to 1 mm total displacement (Section 6.2).

3.4. Fluid flow calculation.

Finally, once that the contact area and geometrical aperture maps were extracted under different normal loads, the flow through the rough fractures was resolved. A finite volume formulation (Crandall et al., 2017; Brush and Thompson, 2003) was used to solve the Reynolds lubrication equation (Reynolds 1886). To apply the Reynolds lubrication equation (here simplified to the local cubic law (Zimmerman and Bodvarsson, 1996)) in the fracture, the main assumption is that the variations in aperture occur gradually in space over the fracture plane. This hypothesis seems reasonable because i) $\frac{h_{RMS}}{\lambda} \ll 1$, thus the vertical variations of roughness with respect to macroscopic wavelength are small, and ii) $\frac{L}{\lambda} > 10$, thus the aperture due to macroscopic wavelength is small compared to the fracture length. The Reynolds boundary layer approximation can therefore be expressed as (Brown, 1987; Zimmerman and Bodvarsson, 1996; Jaeger et al., 2007; Watanabe et al., 2008; 2009):

$$\int_s \rho . [\frac{e_m^3}{12.\mu} . \nabla p] . \hat{n} . dS \ = 0$$

where ρ and μ are the fluid density and viscosity respectively, e_m(x,y) is the local mechanical (or geometrical) aperture in the vertical direction (Brush and Thompson, 2003), S is the domain's surface and $\hat{n}$ is the outward unit normal vector to the local element. Details on the discretization and resolution of the mass conservation equation above can be found in Brush and Thompson, (2003) and Crandall et al. (2017). The imposed boundary conditions on the top and bottom ends of the sample (y-axis) are Dirichlet (constant flow) pressure conditions p_f=$\pm$ 0.15 MPa at y= 0 and p_f=$\pm$ 0.15 MPa at y =L. The sign of the fluid pressures is opposed in all cases and they depend on the flow sense that needs to be applied (top to bottom or bottom to top). Neumann boundary conditions (no-flow) are applied at the lateral fracture boundaries x=0 and x= W. (See Figure 4 for details on the fracture geometry). The results from the finite volume code were validated by comparison with a homemade finite difference code for flow calculation and with a finite element code used with the commercial software Comsol multiphysics® (Annex 2).

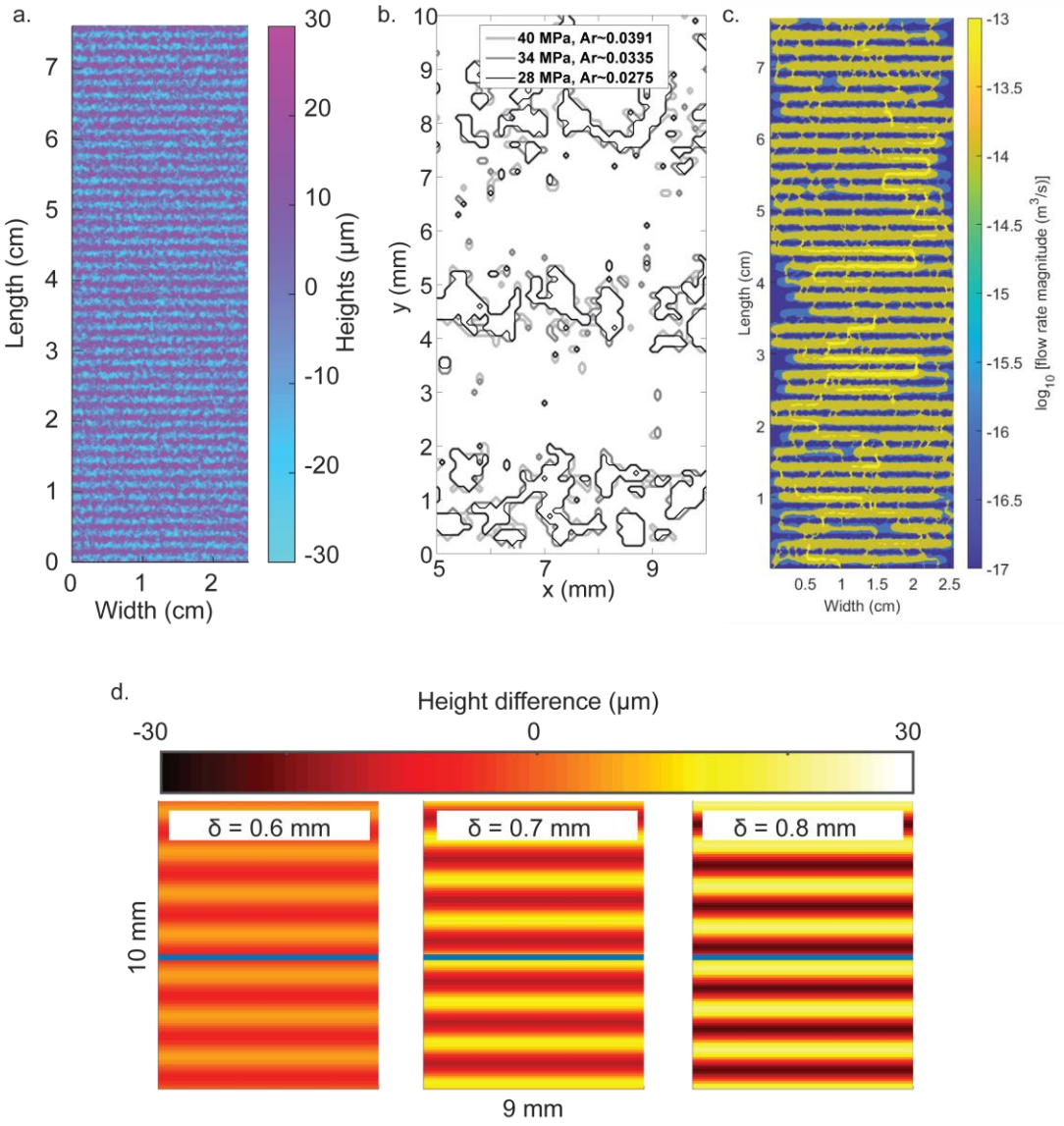

Figure 4. Artificial surfaces: roughness, contact and fluid flow examples. a. Example of one artificially generated surface, colorbar accounts for the height distribution. b. results from contact simulations. Zoom on a 10 mm*5 mm part of the surface representing the contact area between two rough surfaces. Different confining pressures are shown (28, 34, 40 MPa are respectively the black, dark grey and light grey contours) c. Example of a flow through experiment performed with the contact area at σ'_N =28 MPa as input. Colorbar shows the flow rate magnitude through the fracture in logarithmic scale. d. Difference of heights between the initial surface and surfaces

shifted of 0.6; 0.7 and 0.8 mm (left to right panels). Blue bar in the center of the zoomed surface shows a position reference in the middle of the fracture.

While few studies have managed to simulate normal stresses in rough faults followed by the fluid flow through them (Kang et al., 2016), to our knowledge, this is the first study to use a combination of open-source numerical models for i) generating wavy, rough surfaces, ii) simulating the contact under effect of normal stress and iii) the study of fluid flow through the fractures.

4. Experimental results

In all figures, a schematic legend is presented to show the customized sample's roughness. We note that the samples prepared for flow-through experiments under normal loading are not the same as those for experiments under shear loading, thus, slight differences between the sample's roughness can be found for a same nomenclature.

4.1 Fluid flow through single fractures: normal loading.

Figure 5 shows the results of flow-through experiments obtained in terms of transmissivity as function of effective confinement pressure. The dashed lines represent a first cycle where σ_3' was decreased from 40 MPa to 28 MPa (by increasing fluid pressure). The full lines represent a second cycle where the effective confinement was increased from 28 to 40 MPa. Note that the measured transmissivities were always higher when σ_3' was decreased (first loading) than those of the increasing cycle (second loading). To avoid issues related to this hysteretic behavior of the fractures, the transmissivities that will be used hereafter are those of the increasing effective confinement cycle (second loading) because they are representative of the fracture's transmissivity under elastic behavior (Iwai., 1976; Witherspoon et al., 1980; Rutter and Mecklenburgh, 2017; 2018).

The experimental sample M_{LO} (e.g large wavelength sub-orthogonal to fluid flow), showed transmissivities ranging from 3.05e-18 m^3 at σ_3'=28 MPa down to 0.76 e-18 m^3 at σ_3'=40 MPa. Then, M_{SO} (e.g small wavelength sub-orthogonal to fluid flow), showed transmissivities half an order of magnitude smaller than those of M_{LO} (ranging from 0.49e-18 m^3 down to 0.17 e-18 m^3 at σ_3'=40 MPa). The sample with no imposed macroscopic wavelength, M_f had transmissivities ranging from 0.23e-18 m^3 down to 0.15 e-18 m^3. The transmissivities were close to those of M_{LO}

and M_{SO} but the decay with increasing confinement smaller in this experiment with respect to the samples with macroscopic wavelength. The sample M_{LP} (e.g large wavelength sub-parallel to fluid flow), had transmissivities ranging from 0.48e-18 m^3 at σ_3'=28 MPa down to 0.20 e-18 m^3 at σ_3'=40 MPa. The transmissivities were almost half an order of magnitude lower than those of M_{LP} and close to those of M_{SP}.

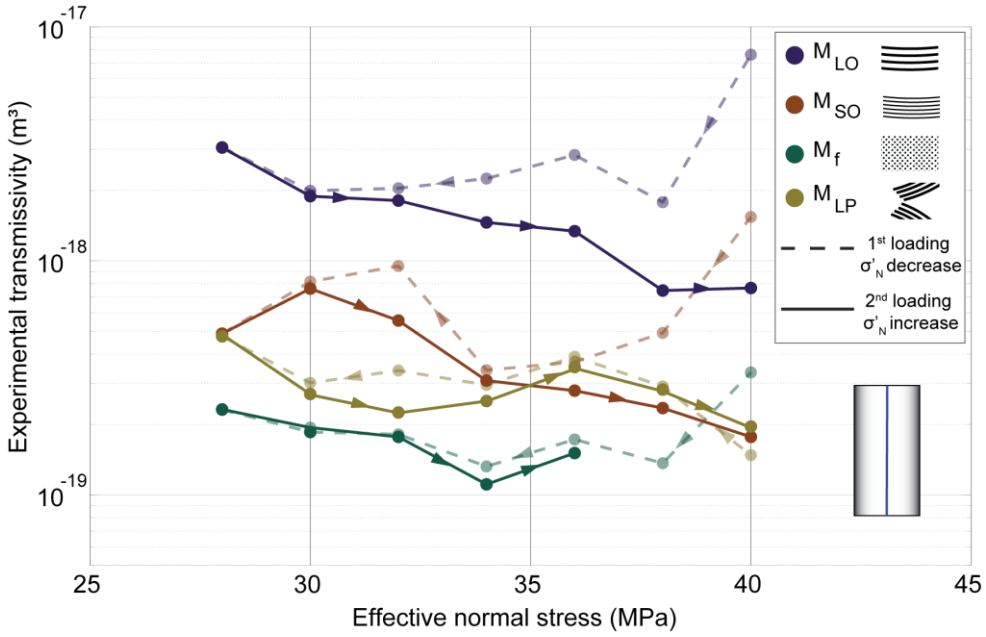

Figure 5. Experimental results of normal loading experiments. Experimental fracture transmissivity function of the applied effective normal stress. Dashed lines represent effective pressure decrease and full lines represent effective pressure increase cycles.

4.2 Fluid flow through single fractures: shear loading.

Stress-displacement evolution.

Figure 6 (left axis) shows the shear stress versus axial displacement curves of all the conducted experiments. In all cases, shear stress first increased elastically (i.e. in a reversible manner) in response to increases in axial piston displacement (notice that due to the fault orientation and loading configuration, the normal stress also increased on the fault during elastic loading). During this stage, the faults were fully locked (Byerlee and Summers, 1975; Ohnaka, 2013; Scholz et al., 1972; Acosta et al., 2019). Then, once the shear strength of the faults was reached, reactivation occurred and shear stress versus displacement curves showed a roll-over (at displacements d_{ro}~0.11 − 0.20 mm) until reaching a steady-state where shear stress stayed

close-to-constant with increasing axial displacement. During this stage, the faults were unlocked and slipped at a near-to-constant rate. It is noticeable that, because axial displacement was increased step-wise to measure transmissivity, the fault showed an increase of shear strength at the start of every new displacement step. This "healing" behavior usually represented less than 10% stress change with respect to fault's shear strength. The peak values of stress and its relaxation are due to the time dependence of the fault's real contact area (Dieterich, 1979; Dieterich and Kilgore, 1994). It is also noteworthy that all samples with an imposed macroscopic wavelength showed a near constant increase in shear stress with displacement after reactivation occurred (Figure 6a,b,d) at friction coefficients (τ/σ_N') close to 0.5 (Table 1). The sample without macroscopic wavelength first showed a (very slow) stress drop at reactivation and then a near-constant increase in shear stress (Figure 6c).

The steady state shear strengths (τ_{ss}) in experiments conducted at $\sigma_3' = 10$ MPa were $\tau_{ss} \sim 14 \pm 2\ MPa$ with a maximum of 15.7 MPa for the sample M_{LO} and a minimum of 12.3 MPa for the sample M_{LP}. At $\sigma_3' = 20$ MPa, τ_{ss} were in the range of 24 ± 3 MPa with a maximum of 27.0 MPa for M_{LO} and a minimum of 22.0 MPa for M_{LP}. The steady state effective normal stress in experiments conducted at σ_3'=10 MPa ranged from 34.0 to 37.5 MPa. At σ_3'=20 MPa the effective normal stresses on the fault ranged from 58.7 to 66.3 MPa. As a result, all the experiments presented state friction values in the range $f_{ss} \sim 0.54\ to\ 0.61 \pm 0.02$, in agreement with Byerlee's Rule (Byerlee, 1978). A compilation of the values is given in Table 1.

Transmissivity results.

The transmissivities measured during shear loading experiments are shown in Figure 6 (right axes). In experiments conducted at σ_3'=10 MPa, the initial transmissivities (kt_0; e.g. with no applied deviatoric stress and at zero axial displacement) ranged from ~$2.33.10^{-16}$ to $2.42.10^{-18}$ m^2 with maxima and minima for samples M_{LO} and M_{LP} respectively. With increasing axial displacement, transmissivity sharply decreased during reversible fault loading (usually of more than one order of magnitude). For the experiments M_{LO} and M_{LP}, it dropped to values of $1.27.10^{-17}$ and $2.60.10^{-19}$ m^2 respectively (e.g. of ~1 order of magnitude) at the onset of reactivation respectively. During fault reactivation, transmissivity usually slightly decreased overall; with local rises (to kt_{ss}^{max}) and drops (to kt_{ss}^{min}) of lesser magnitude than the decrease during elastic loading. Finally, after unloading, transmissivity (kt_{unl}) slightly increased in most cases (Except for sample M_{LP} deformed at $\sigma_3' = 20\ MPa$) but was far from being recovered to

454 kt_0. Transmissivity after unloading was usually close to the value found at the onset of
455 reactivation. For experiments conducted at σ_3'=20 MPa, kt_0 were 3 to 42 times larger than at
456 σ_3'=10 MPa (except for M_{LP} where kt_0 was surprisingly two orders of magnitude higher at σ_3' =
457 20 MPa). At the onset of reactivation, $kt_{ss}(\sigma_3' = 20$ MPa) were 13 to 392 times lower than kt_{ss}
458 at σ_3'=10 MPa). Finally, at unloading kt_{unl} was 11 to 105 times lower at larger confining stress.

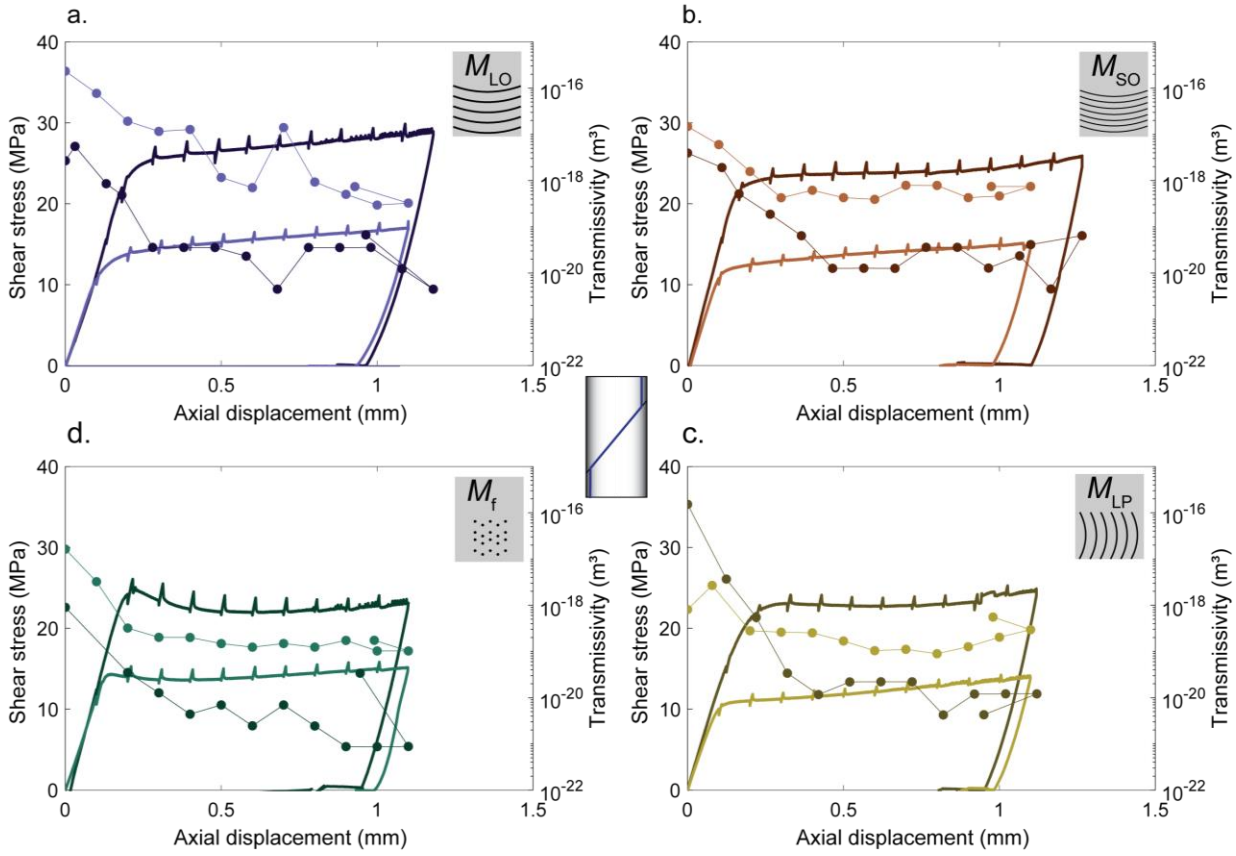

459

460 Figure 6. Coupled evolution of fault's shear stress and transmissivity in response to shear
461 loading. In all panels, left y-axis shows shear stress (note that normal stress also increased during
462 shear loading), right y-axis shows fault's transmissivity (circles) and x-axis is the axial
463 displacement. Darker and lighter colors represent experiments conducted at 20 and 10 MPa
464 effective confinement pressure respectively. a. Experiments on sample M_{LO} (long wavelength,
465 grooves sub-orthogonal to fluid flow and shear displacement). b. Experiments on sample M_{SO}
466 (small wavelength, grooves sub-orthogonal to fluid flow and shear displacement). c. Experiments

on sample M_f (with no macroscopic imposed wavelength). d. Experiments on sample M_{LP} (long wavelength, grooves sub-parallel to fluid flow and shear displacement).

5. Microstructures

5.1 Initial sample roughness.

Figure 7 shows the PSD curves for all initial experimental surfaces. The 2D PSD curves presented 2 sections: A first, 'flat' part where the power spectral density was close to constant with increasing wavenumber until the roll off wavenumber q_r. And a second part, presenting a power law dependence on wavenumber. The slope in a log-log plot is $-2.(H+1)$ with H the Hurst exponent (Candela et al., 2012; Jacobs et al., 2017). The Hurst exponent characterizes the power law decay of PSD with increasing wavelength. In that sense, H usually characterizes the fractal dimension of a surface (Candela, 2012; Jacobs et al., 2017 and references therein). Finally, the area under the PSD curves represents the Root Mean Square height (h_{RMS}) which is the standard deviation of the heights distribution (Candela., 2012; Jacobs et al., 2017 and references therein).

Prior deformation, for $q< q_r$, the samples M_{LO} had amplitudes (C($q<q_r$) ~ 2.10^{-19} m^4), and the samples M_{SO} and M_{LP} had smaller amplitude prior to roll off (C($q<q_r$) ~7-8.10^{-20} m^4). Finally, the sample with no macroscopic wavelength -M_{f}- had the smallest amplitudes prior to roll-off (C($q<q_r$) ~1.10^{-20} m^4). The roll of wavenumbers were the smallest for M_{LO}, M_{LP} and M_{SO} (q_r~6900 rad.m^{-1}). q_r were larger for the sample with no macroscopic wavelength M_{f} (q_r~10000 rad.m^{-1}) (Table 1). Regarding Hurst exponents determined from the slope of the PSD curves, the samples M_{LO} and M_{SO} had H respectively 0.47 and 0.60. The sample with no macroscopic wavelength M_{f} had lower H~0.44 and finally M_{LP} had H~0.59. The largest h_{RMS} were calculated for M_{LO} and M_{SO} (~9.0 and 8.0 μm respectively). Then, M_{f} had lower h_{RMS} ~4.5 μm and finally M_{LP} had h_{RMS}~7.5 μm. The sample M_{LO} had a macroscopic wavelength λ= 1.7 mm with while the M_{SO} surfaces had λ= 0.9 mm. Both samples had an imposed wavelength amplitude of 11 μm. Finally, M_{LP} had λ= 1.7 mm with an amplitude of ~9 μm. The results are summarized in Table 2.

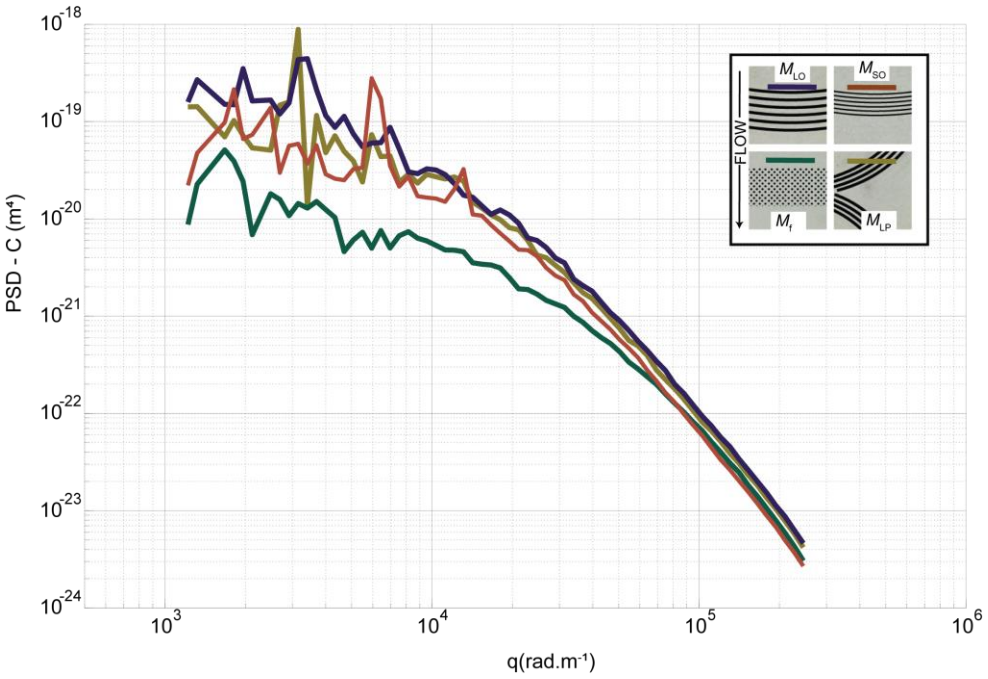

Figure 7. Results of surface roughness measurements for all the experimental samples. 2D-Power spectral density of height distribution. Insets show which sample corresponds to which PSD curve.

5.2 Post-deformation sample roughness.

Fault surface roughness changed when shear displacement increased. The topography maps after deformation are shown in Figure 8 (at low confining pressure in panels a-d and at high confining pressure in panels e-h). Note that a different sample was used for each confining pressure experiment so as to initiate loading in similar conditions. Overall, the post-mortem samples showed evidence of striation (grooves in the sense of shear), as well as changes in the height distributions (Figure 8). Evidence was found of gouge formation during shearing with pervasive presence of microscopic particles in low height zones. Larger amounts of gouge were generated in experiments at higher confining pressure. It is noticeable that at both effective confinements, the samples M_{LP} (e.g. with grooves sub-parallel to the shear sense), showed very large changes in the surface characteristics (Figure 8d,h). There, the initial wavelengths were unrecognizable from topography measurements while in all the other experiments, the initial surface topography could be partly recognized.

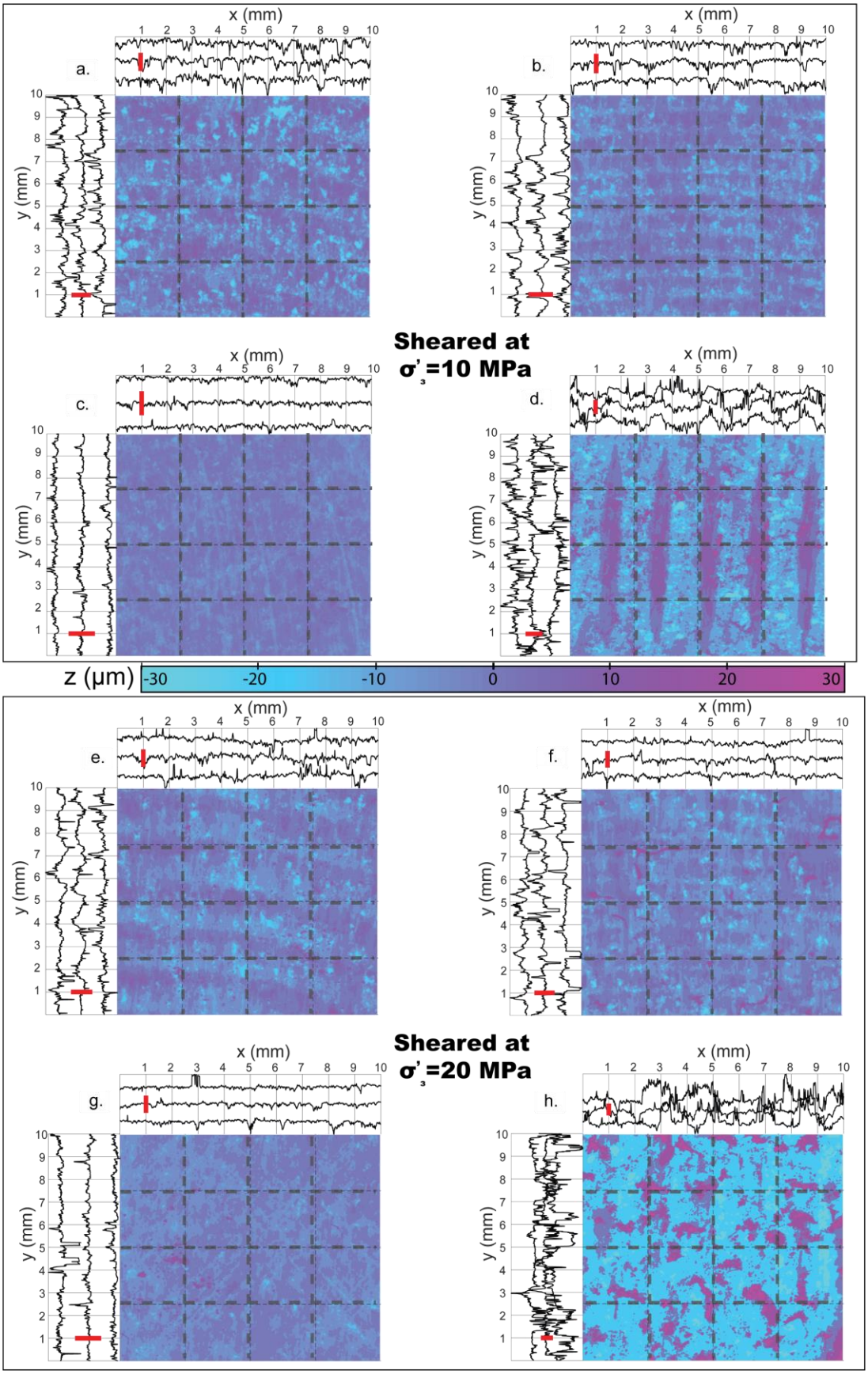
a.
b.
c.
d.
e.
f.
g.
h.
x (mm)
y (mm)
Sheared at
σ'3=10 MPa
Sheared at
σ'3=20 MPa
z (μm)
-30
-20
-10
0
10
20
30

Figure 8. Post-mortem surface topography maps. Colorbar represents the measured heights over the area. The transects in x-axis and y-axis in dotted lines are presented in the top and left plots respectively. For reference, a red bar represents 30 micrometer height. a-d Maps of post-deformation experiments at 10 MPa effective confinement for samples M_{LO} (panel a.); M_{SO} (panel b.); M_f (panel c.); M_{LP} (panel d.); e-h Maps of post-deformation experiments at 20 MPa effective confinement for samples M_{LO} (panel e.); M_{SO} (panel f.); M_f (panel g.); M_{LP} (panel h.). Surface topographies can be compared with Figure 1a-d.

To study the statistical properties of these surfaces, the PSD's were computed again on post-mortem topography maps and analyzed in the same manner as those of intact surfaces. The PSD curves showed a change in shape. Indeed, the previously 'flat' part of the PSD's showed an overall slope after deformation, adding additional complexity to the estimation of the roll-off wavevector for post-mortem samples. The results are compiled in Table 3 and summarized in Figure 9. The root mean square of heights h_{RMS} decreased after shearing in all cases (except for the sample M_{LP} deformed at σ_3' 30 MPa) (Figure 9a). No tendency was observed regarding h_{RMS} with respect to the confining pressure at which the samples were deformed. q_r was here estimated where the slope of the PSD curves changed. With that estimation of q_r, an overall decrease was observed for all samples after shearing with the measurements converging on all samples towards values of $\sim 5000 - 8000$ rad.m^{-1} (Figure10b). Finally, the Hurst exponent also showed an overall decrease after shearing for all samples with slightly lower values of H in experiments at higher effective confinement (Figure 9c).

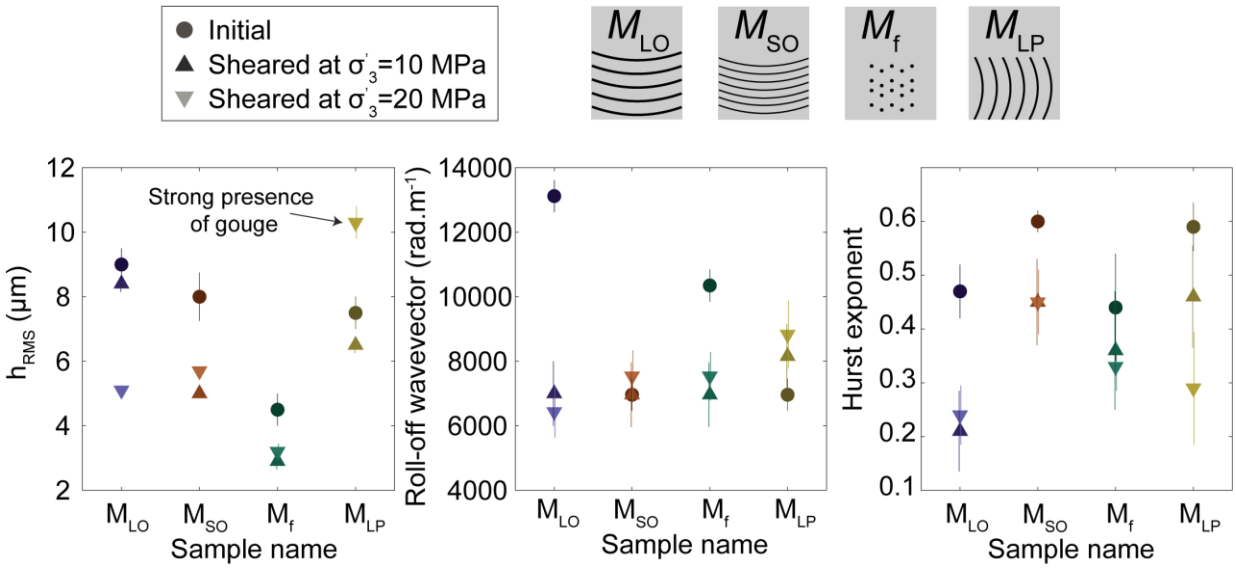

Figure 9. Pre-and-post-mortem roughness parameters. Circles represent initial surfaces with the estimated error. Upward triangles represent post-mortem samples deformed at 10 MPa effective confinement and downward triangles represent experiments at 20 MPa effective confinement. a. root mean square of heights parameter. b. roll-off wavevector. c. Hurst exponent.

Sample	Grooves[a]	Deformed	σ'_3	λ[b]	$^{err}\lambda$[c]	Amp[d]	^{err}Amp[c]	h_{rms}[e]	$^{err}h_{rms}$[f]	q_r[g]	$^{err}q_r$[h]	H[i]	^{err}H[j]
name	∥,⊥,no		MPa	mm	mm	μm	μm	μm	μm	$rad.m^{-1}$	$rad.m^{-1}$	-	-
M_{LO}	⊥	intact	0	1.7	0.1	11	2	9	1	6963	1000	0.47	0.1
M_{SO}	⊥	intact	0	0.9	0.1	11	2	8	1.5	6963	1000	0.6	0.04
M_f	no	intact	0	0	0	0	0	4.5	1	10350	1000	0.44	0.2
M_{LP}	∥	intact	0	1.7	0.1	11	2	7.5	1	6963	1000	0.59	0.09
M_{LO}	⊥	sheared	10	1.7	0.1	15	5	8.4	0.5	7000	2000	0.21	0.15
M_{SO}	⊥	sheared	10	0.9	0.1	15	5	5	0.2	6963	2000	0.45	0.16
M_f	no	sheared	10	0	0	0	0	2.9	0.5	6963	2000	0.36	0.22
M_{LP}	∥	sheared	10	0	0.1	17	5	6.5	0.5	8158	2000	0.46	0.19
M_{LO}	⊥	sheared	20	1.7	0.1	15	5	5.1	0.3	6433	1600	0.24	0.11
M_{SO}	⊥	sheared	20	0.9	0.1	15	5	5.7	0.2	7537	1600	0.45	0.12
M_f	no	sheared	20	0	0	0	0	3.2	0.5	7537	1500	0.33	0.09
M_{LP}	∥	sheared	20	2	0	35	10	10.3	1	8831	2100	0.29	0.21

[a] parallel or orthogonal to fluid flow
[b] determined by counting the number of wavelengths in a given area
[c] determined from the difference between the six prepared half-samples
[d] determined from the roughness profiles
[e] determined from the integral of radially averaged 2D-PSD and from the standard deviation of heights
[f] determined from the differences between intergral of radially averaged PSD and from the standard deviation of heights and the 6 half samples
[g] determined from the flat part of radially averaged PSD
[h] determined from the difference between the 6 prepared half samples
[i] determined from the self-similar part of radially averaged PSD
[j] determined from the difference between the 6 prepared half samples and from the maximum and minimum slope taken on a moving window of half an order of magnitude

Table 2. Experimental samples roughness.

6 Discussion.

6.1 Influence of roughness parameters on fracture transmissivity under normal loading.

The hydraulic transport properties of rough fractures submitted to normal stress are highly dependent on the surface geometry and roughness parameters (Section 4.2; Chen et al., 2000; Watanabe et al., 2008; 2009; Patir and Cheng, 1978; Iwai, 1976; Pyrak-Nolte et al., 1988; Walsh, 1981; Watanabe et al., 2008; 2009; Iwai, 1976; Witherspoon et al., 1980; Rutter and Mecklenburgh, 2017; 2018). We now study the flow through wavy rough fractures submitted to normal loading only in this subsection. As described in section 3, first artificial surfaces with roughness parameters similar to those measured experimentally were generated. Then, the contact between the surfaces at given loads was simulated, and finally the flow through the fractures was computed. The numerical results are presented in Figure 10a corresponding to the samples tested experimentally. For all samples, two types of numerical simulations were conducted. One where the large wavelengths were in peak-to-peak contact (e.g non-mated or non-imbricated surfaces, Figure 10 triangles). In those cases, the resolved numerical transmissivities were more than two orders of magnitude larger than those measured experimentally (Figure 5). Another set of numerical simulations was conducted where the large wavelengths were in peak-to-valley contact (e.g fully mated surfaces, Figure 10a circles). In this case, the resolved numerical transmissivities ranged from 0.50e-18 m^2 at σ_3'=28 MPa down to 0.20e-18 m^2 at σ_3'=40 MPa, for sample M_{LP} as an example. The fully mated transmissivity results are in strong in compatibility with experimental results. This highlights the strong influence of flow channeling on fracture hydraulic transport capacity which cannot be neglected in the analysis (Watanabe et al., 2009; Shvarts and Yastrebov., 2018; Shvarts, 2019).

We observe that for all samples, the numerical transmissivity has an exponential decay with increasing normal stress (the plot is log-normal) as as $kt(\sigma_N') = a.e^{-b\sigma_N'}$, with a and b two fitting parameters. The sample's initial geometry seems to condition the parameters a and b. With larger values of the b parameter in samples M_{LO} ($b_{M_{LO}}$=0.190) and M_{SO}($b_{M_{SO}}$=0.198). Then, an intermediate value of b is found for sample M_f (b_{M_f}=0.103) and the smaller one for M_{LP} ($b_{M_{LO}}$=0.099). To summarize, samples with grooves perpendicular to fluid flow are more sensitive to normal stress than samples with no roughness which are in turn more sensitive than samples with grooves sub-parallel to fluid flow. The transmissivity decay with increasing normal

stress has been seen with i) near exponential decays (Iwai, 1976; Witherspoon et al., 1980; Pyrak-Nolte et al., 1988), ii) logarithmic decay (Walsh, 1981), or iii) through more complex decays depending on heterogeneous topographies (Watanabe et al., 2008; 2009) and loading paths (Iwai, 1976; Witherspoon et al., 1980; Rutter and Mecklenburgh, 2017; 2018).

From the numerical procedure developed in this work, one can expect a near exponential decay of transmissivity at the working experimental normal stresses for the modeled carbonate rock. In turn, the experimental results show a small scatter towards the exponential decay predicted by the model. Which can be due to i) the loading path (e.g. hysteresis; Iwai, 1976; Witherspoon et al., 1980; Rutter and Mecklenburgh, 2017; 2018); ii) imperfections in the experimental contacts with respect to the numerical model; or iii) small non-linearities in fluid flow in real sample surfaces (Zimmerman and Bodvarsson., 1996) which are not considered in the Reynolds lubrication approximation for the simulations. Overall, the numerical results are remarkably consistent with the experimental data, as shown by the small deviation of data from the 1:1 slope in Figure 10b. In the numerical simulations, more than 90% of the points are contained within a factor 2.5 from the experimental data.

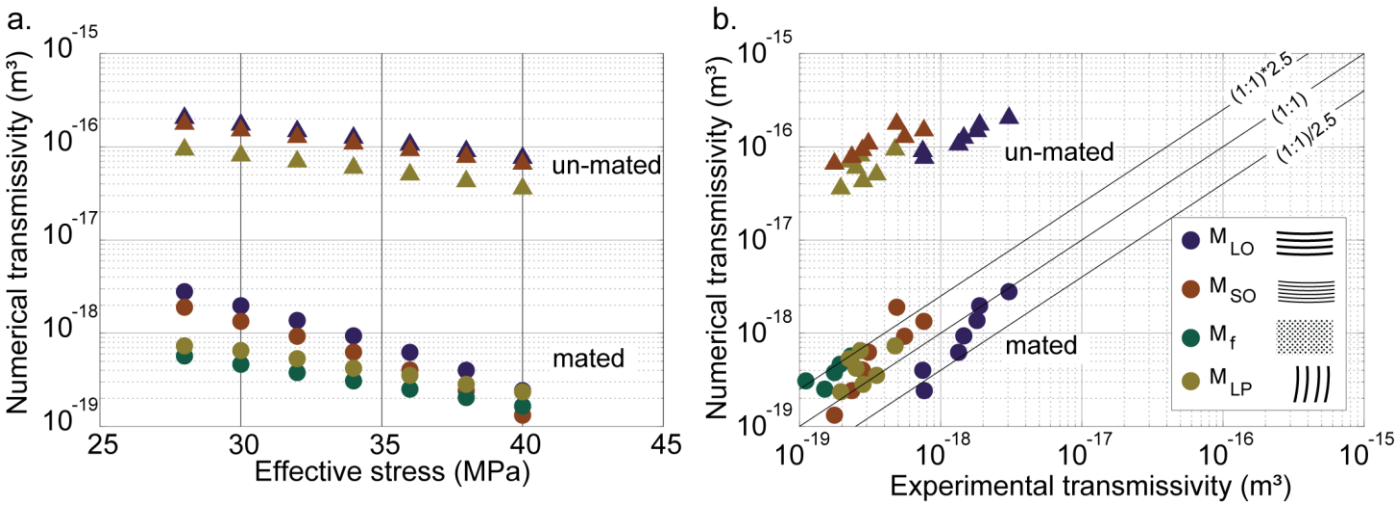

Figure 10. Flow through numerical results. a. Numerical fracture transmissivity function of effective stress applied on the fracture. b. Numerical transmissivity function of experimental transmissivity. In both panels, triangles represent the numerical results from samples with an un-mated configuration. In panel b. the black lines represent a slope of 1 and a deviation with a factor 2.5 to that line. Note that more than 90 % of the data points were contained within that factor. The numerical model developed gives good agreement with the experimental hydraulic transport properties measured under normal loading.

The goal of the following section is to isolate the roughness parameters that have stronger control on hydraulic transport properties through a parametric analysis of the numerical procedure. First, the parameters are isolated in absence of macroscopic grooves and then, the effect of the large-scale wavelength with grooves perpendicular to the fluid flow is studied.

Flat rough surfaces (absence of macroscopic grooves)

First, the roughness properties are analyzed for rough surfaces without imposed wavelength to avoid bias from the macroscopic grooves on all other parameters ($H; q_r; h_{RMS}$). Artificial surfaces with L = 75 mm (length) and W =25 mm (width) with 768*256 nodes were created and tested through the same numerical procedure described in section 3. The steady parameters (the parameters that do not change when only one of the other parameters is varied) are H = 0.6, q_r = 8000 rad.m^{-1} and h_{RMS} = 8 μm. Hurst exponents are varied from 0.5 to 0.9 (values that can be found in natural and experimental faults; Brown and Scholz, 1985; Candela et al., 2009), roll-of wave-vectors are varied from 1000 to 10000 rad.m^{-1} and h_{RMS} are varied from 2 to 8 μm. Results are shown in Figure 11.

- The Hurst exponent characterizes the power law decay of PSD with increasing wavelength. Thus, it characterizes the self-affinity of a surface (Candela, 2009; Renard et al., 2013; Jacobs et al., 2017 and references therein). Changes from 0.5 to 0.9 in Hurst exponent alone (Figure 11a), do not show large changes in transmissivity (30 to 60 % lower for the lowest tested Hurst exponent) of the simulated fractures.
- q_r is the wave-vector where the PSD curves change from a close-to-constant value to a power law distribution with increasing wavenumber (with a power $-2(H+1)$). Physically this number represents the wavevector where the surface heights depart from a self-affine distribution. From Figure 11b, q_r has a strong influence on transmissivity only for q_r< 5000 rad.m^{-1}. Under our experimental conditions q_r is often comprised between 5000 and 10000 rad.m^{-1} (Table 3). In that range, q_r variation has little influence over the transmissivity response.

- The root mean square of the height distribution (h_{RMS}) corresponds to its standard deviation, thus to the dispersion of heights around the mean value. The higher h_{RMS}, the 'rougher' the surface (Brown and Scholz, 1985, Candela et al., 2009; 2012; Renard et al., 2013; Jacobs, 2017) and the higher the hydraulic apertures. From Figure 11c, we observe that h_{RMS} has the largest influence over the transmissivity response of the flat-rough fractures. Increase of 2 to 8 μm results in over three orders of magnitude difference transmissivity. The lower h_{RMS} height, the flatter the surfaces, hence, under normal load, the better they match to each other and the smaller their mechanical and hydraulic apertures.

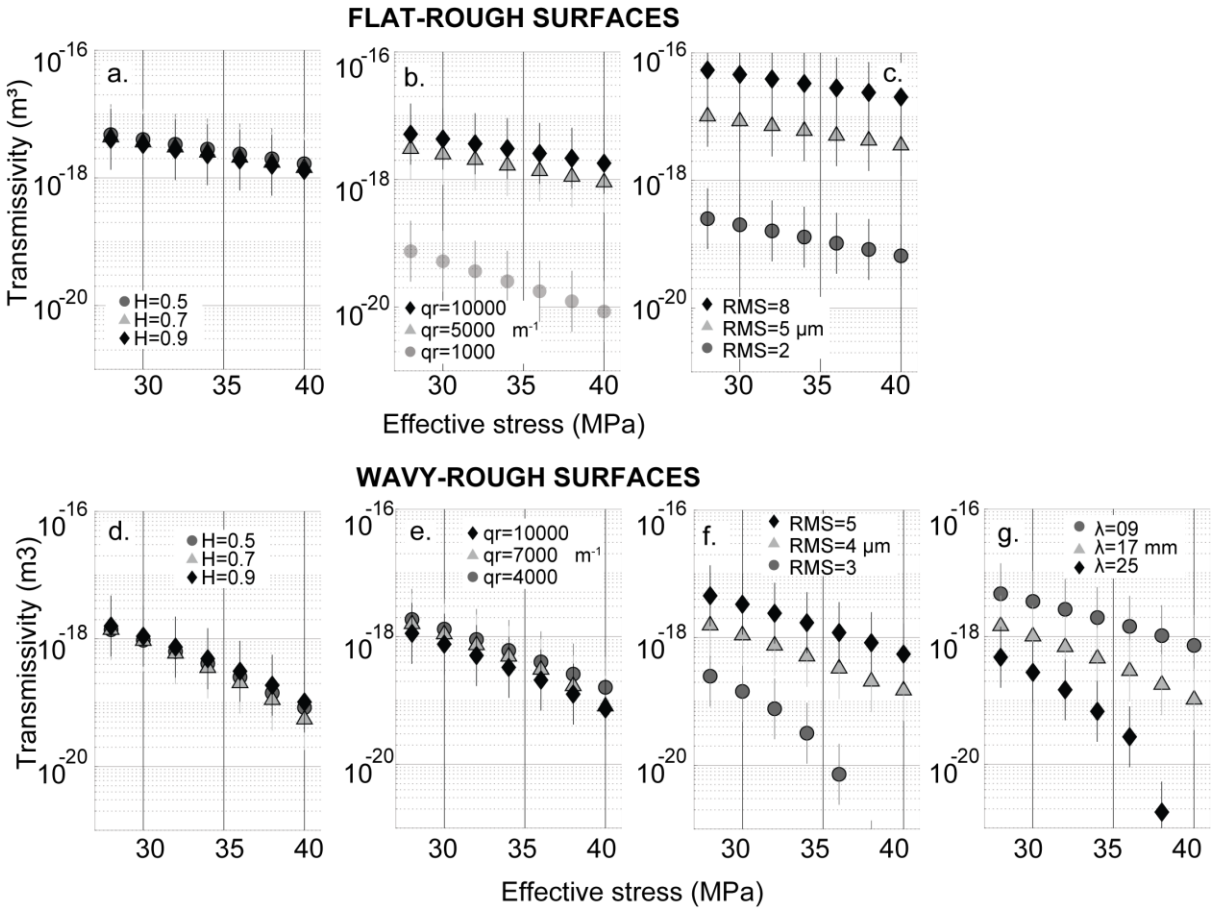

Figure 11. Parametric analysis. a-c. For flat rough surfaces. All panels show fracture transmissivity function of the simulated effective stress. Error bars correspond to a factor 2.5 in transmissivity which is taken as model's accuracy. a. Variation of the Hurst exponent alone. b. Variation of the roll-off wave vector alone. Note that a wavevector of 1000 rad.m^{-1} is widely out of the range from experimental samples. c. Variation of h_{RMS}. The base values for this

parametric analysis are given in the text. e-g. Parametric analysis for wavy-rough surfaces. a. Variation of the Hurst exponent alone. b. Variation of the roll-off wavevector alone. c. Variation of the whole h_{RMS}. d. Variation of the macroscopic wavelength. The base values for this parametric analysis are given in the text.

Wavy rough surfaces (in presence of macroscopic grooves)

To study the effect of the macroscopic wavelength on fracture's transmissivity, artificial surfaces were generated by overlaying a surface with a macroscopic wavelength and a flat rough surface such that the overall h_{RMS} equals the targeted value. The steady parameters are H = 0.6, q_r = 7000 rad.m^{-1} and h_{RMS} = 4 μm and wavelength λ = 1.7 mm. These reference values are taken from experimental observations. Hurst exponents are varied from 0.5 to 0.9, roll-of wave vectors are varied from 4000 to 10000 rad.m^{-1}, h_{RMS} are varied from 3 to 5 μm and wavelengths λ from 0.9 to 2.5 μm. Results are shown in Figure 11d-g.

Figures 11d,e show again that H and q_r alone have little influence on the transmissivity of wavy rough surfaces (changes of 30 to 60% in transmissivity for a change of 0.4 in H and 3 to 5 times increase in transmissivity for a variation of 6000 in q_r). On the other hand, h_{RMS} has strong control on the fracture's transmissivity (Figure 11f). Indeed, at σ_3' = 35 MPa, the transmissivity is more than 3 orders of magnitude larger from h_{RMS} ~ 3 μm to 5 μm. We observe that for a change in λ from 0.9 to 2.5 cm, at σ_3'= 35 MPa, the increase in transmissivity is more than 3 orders of magnitude (Figure 11g) highlighting the strong control of the wavelength on the hydraulic transport capacity of the rock fracture.

We performed thirty-six additional simulations to explore the combined effects of wavelength and standard deviation of heights on fracture's transmissivity (these simulations were performed with $\sigma_N' = 28$ MPa as an example). The results are shown in Figure 12. The evolution of transmissivity is strongly non-monotonic in the parameter space. A combination of small λ and low h_{RMS} naturally results in low transmissivities. Nevertheless, low λ (500 -1000 μm) and intermediate h_{RMS} (10 μm) can result in regions of lower transmissivities than its surroundings. At intermediate λ (~1500 μm), an increment of h_{RMS} results in less increase in transmissivity than at higher λ (~2100 μm) for example. We conclude from this analysis that, for complex topographies, the transmissivity of wavy rough fractures from averaged height values (h_{RMS} only for example) needs to be evaluated with care (Renshaw, 1995; Zimmerman and

Bodvarsson., 1996; Brown, 1987; Hakami, 1989; Piggott and Ellsworth., 1992; Patir and Cheng, 1978).

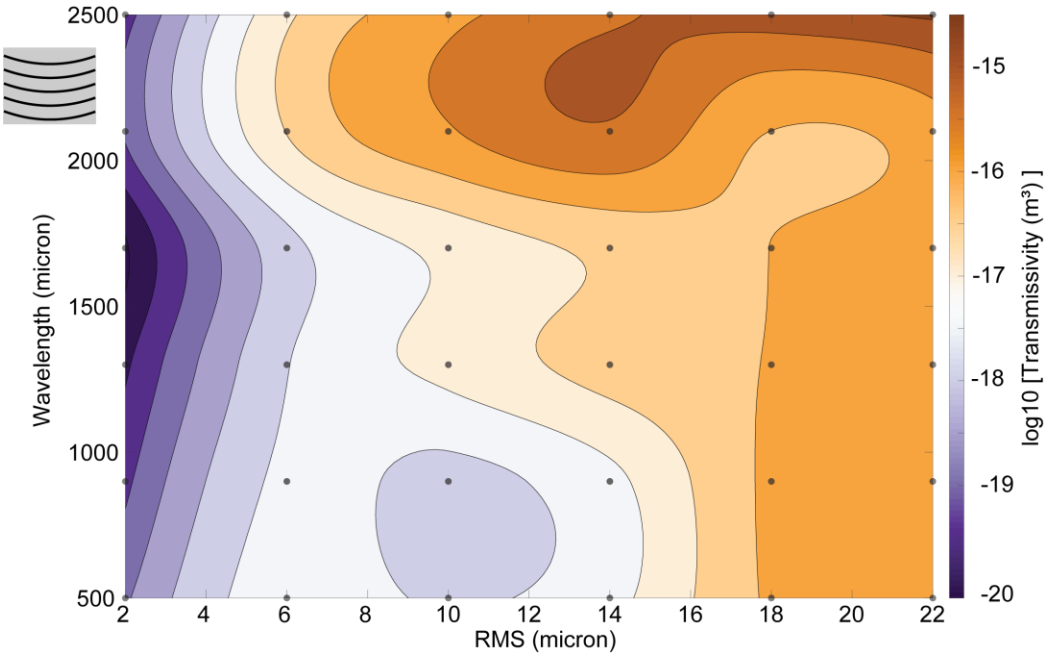

Figure 12. Contour plot of transmissivity of rough wavy surfaces (grooves sub-orthogonal to fluid flow). The fault's transmissivity (in log scale) is computed as function of the root-mean-square roughness (h_{RMS}) and the macroscopic wavelength for artificial wavy-rough surfaces. Effective pressure considered for this plot is 28 MPa.

6.2 Influence of reversible shear loading and of irreversible shear displacement on transmissivity.

The effect of reversible shear loading on transmissivity (prior the onset of sliding).

Elastic shear loading strongly decreased transmissivity under all tested conditions. The change in transmissivity is due to the increase in both normal and shear stress on the fracture prior to sliding (note that this type of loading is more common in natural faults than a shear loading at constant normal stress). In order to isolate the effect of reversible shear load, we now compare the results from the validated numerical model (for fractures submitted to normal stress only) to the experimental results obtained under both shear and normal stress. To do this, the model results of fracture transmissivity function of normal stress were fitted with an exponential

decay as $kt(\sigma'_N) = a.e^{-b\sigma'_N}$ (full colored lines in Figure 13). The values of a and b are given in Figure 13. Then, we compare the model values to experimental results of fracture transmissivity submitted to both normal and shear stress during reversible (elastic) loading (filled circles in Figure 13; darker colors for higher effective confinement). Note that all deviations from the (normal loading) model results from the effect of shear loads shear loads in this configuration. We observe that reversible shear load has very little effect on transmissivity. It either increases or decreases fault transmissivity with respect to the case where only normal load was applied. When the sample had no macroscopic roughness (M_f, Figure 13c), the transmissivity mostly decreased, in particular when high (normal and shear) stress was applied. Similar observations were observed previously in smooth hard-rock surfaces at high stresses (Rutter and Mecklenburgh, 2017; 2018). In the case of sample M_{LO} (Figure 13a), transmissivity rose of almost two orders of magnitude under all stress conditions. For sample M_{SO} (Figure 13b), transmissivity was not affected by shear stress at low confinement (first two points from left to right) but increased at high confining pressure (3rd and 4th points from left to right). Finally, for sample M_{LP} (Figure 13d), the transmissivity usually decreased except for one point that seems to be an outlier in the transmissivity evolution (Figure 6d, displacement < 0.1 mm).

An increase in transmissivity due to the application of reversible shear load alone should be due to a decrease of the real contact area with increasing shear stress because the hydraulic aperture (h_H) is a function of the real contact area (A_r) as (Walsh, 1981):

$$h_H = h_M.\left(\frac{1 - A_r}{1 + A_r}\right)^{\frac{1}{3}}$$

where h_M is the geometrical aperture of the fracture surface. The evolution of the real contact area with increasing shear in a frictional contact is today a controversial issue in the contact mechanics community. On the one hand, several studies have shown a decrease of the real contact area with increasing shear stress prior to (and at the onset of) sliding in mortar rock replicas (Grasselli and Egger, 2003; Park and Song, 2013); on hard polymers (BenDavid et al., 2010; Svetlizky and Fineberg, 2014; Bayart et al., 2016); and on soft polymers (Sahli et al., 2018). On the other hand, experiments in hard, coated polymers (Bay and Wanheim, 1976) and in polystyrene-on-glass contacts (Weber et al., 2019) have shown that the real contact area in turn increases with shear stress and initial displacement due to a mechanical degradation of the asperities (plastic deformation). By isolating the effect of normal stress and shear stress

719 separately on transmissivity, our results show that the application of reversible shear load is not
720 the only factor affecting fracture transmissivity but rather the combination of geometry and
721 stress, even though its effect is small. Indeed, both samples with macroscopic grooves sub-
722 orthogonal to shear showed the largest increase of transmissivity. In experiments similar as those
723 conducted here but in smooth, hard- rock samples (Rutter and Mecklenburgh, 2017; 2018), the
724 increase of shear stress at constant normal stress led to a very slight decrease in fault
725 transmissivity at the onset of reactivation. There, the authors inferred that the slight
726 transmissivity decrease was due to asperity collapse during shear loading. In our experiments, it
727 seems therefore reasonable that during elastic loading only (e.g. while no permanent changes in
728 surface topography occur), the transmissivity varies very little with increasing, reversible shear
729 load.

730 From this analysis, we conclude that the stress state alone does not fully determine the
731 hydraulic transport capacity of a rock fracture. It seems that there is an interplay between fracture
732 geometry and the state of stress (shear and normal stress applied on the fracture) that determines
733 fracture transmissivity. To examine the exact contribution of shear stress applied on the fracture,
734 more complex elastic-plastic models are required. First attempts going in this direction are the
735 models of Yastrebov et al. (2017) and those of Shvarts and Yastrebov (2018a, ;2018b) where the
736 problem is approached through spectral boundary element methods. These methods should
737 allow, in term, the extension to shear stress and plasticity (Frerot et al., 2019) with the
738 geometries used in this study (grooves sub-orthogonal to fluid flow and shear sense as well as
739 parallel ones).

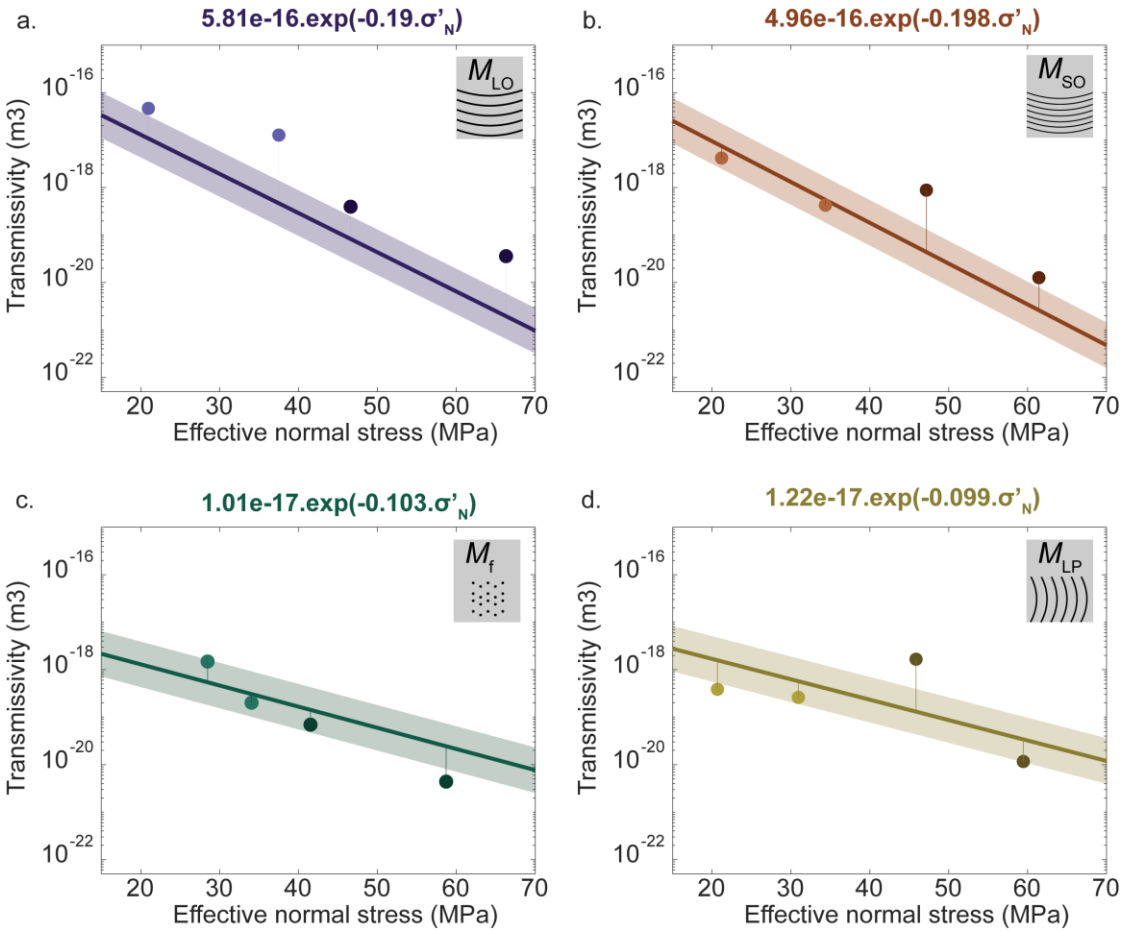

Figure 13. The contribution of reversible shear stress to fault transmissivity. All panels show Transmissivity vs. effective stress applied on the fracture. Full colored lines represent the exponential fit from the calibrated numerical models of transmissivity in faults submitted only to normal stress. The shaded areas represent the estimated error associated to the model. Circles represent the measured value of transmissivity under both normal and shear stress. Vertical lines show the difference between the two values at the experimental measured normal stress at the onset of reactivation. The vertical lines show therefore the contribution of shear stress to transmissivity. panels a; b; c; and d represent the samples M_{LO}; M_{SO}; M_f; and M_{LP} respectively. Darker and lighter colors represent experiments conducted at 20 and 10 MPa effective confinement pressure respectively.

The effect of (irreversible)shear displacement.

Once that irreversible shear displacement started and the fault reached a 'steady state' sliding condition, with near constant shear and normal stresses, the fault's transmissivity varied

only slightly, usually of less than one order of magnitude (Figure 6). Our experimental results of change in transmissivity during shear sliding are plotted as full lines (with empty circles as markers, left y-axes) in Figure 14. There, transmissivity is normalized by the mean fracture transmissivity during shear sliding.

In order to isolate the effect of increasing shear displacement from the effect of normal loading on fracture's transmissivity (through the use of the numerical model), the shear problem is simplified. To do it, the wavy rough surfaces are simply shifted of a given displacement, and then the normal loading and fluid flow models are applied (See section 3.3 for details; and Figure 4d) with no shear loading nor wear components. In this case, the applied load on the shifted fracture surfaces corresponds to the mean experimentally measured normal stress during shear sliding ($\sigma'_{N_{ss}}$ in Table 1). The numerical results from the model are plotted as thick transparent areas (with filled triangles as markers, right y-axes) in Figure 14. Again, the values are normalized by the mean fracture transmissivity during shear sliding. On the one hand, in experiments conducted at low confining pressure (σ'_3 = 10 MPa; Figure 14a-d), the general tendency of transmissivity change is fairly well captured by the simplified model even though the absolute values can be off by more than an order of magnitude. On the other hand, at high confining pressures (σ'_3 = 20 MPa; Figure 14e-h), the simplified model is far from capturing the tendency of transmissivity change with ongoing shear slip. We interpret these differences at low and high confining pressure as due to strong changes in surface roughness (due to plastic deformation and wear) with ongoing slip. Indeed, the model presented here is extremely simplified because it does neither consider the evolution of an applied shear stress on the fracture's macroscopic wavelengths nor the production of wear particles (Aghababaei et al., 2016; Milanese et al., 2019; Molinari et al., 2018). The plasticity (Frerot et al., 2019) and wear (Archard., 1953; Molinari et al., 2018) processes should be enhanced by higher applied normal and shear stresses, thus generating larger changes in surface topography in our experiments at high confining pressures. In turn, the generation of a third body during frictional sliding is expected to highly contribute to i) the frictional sliding process (a review is given in Scholz, 2019) and ii) the fracture transmissivity (Faoro et al., 2009; Tanikawa et al., 2010; Rutter and Mecklenburgh., 2017; 2018).

784 We note that, a more refined model should consider not only the deformations due to
785 shear stress (Park and Song, 2013) but mostly to wear processes and the formation of a third
786 body (Aghababaei et al., 2017; Milanese et al., 2019; Molinari et al., 2018).
787

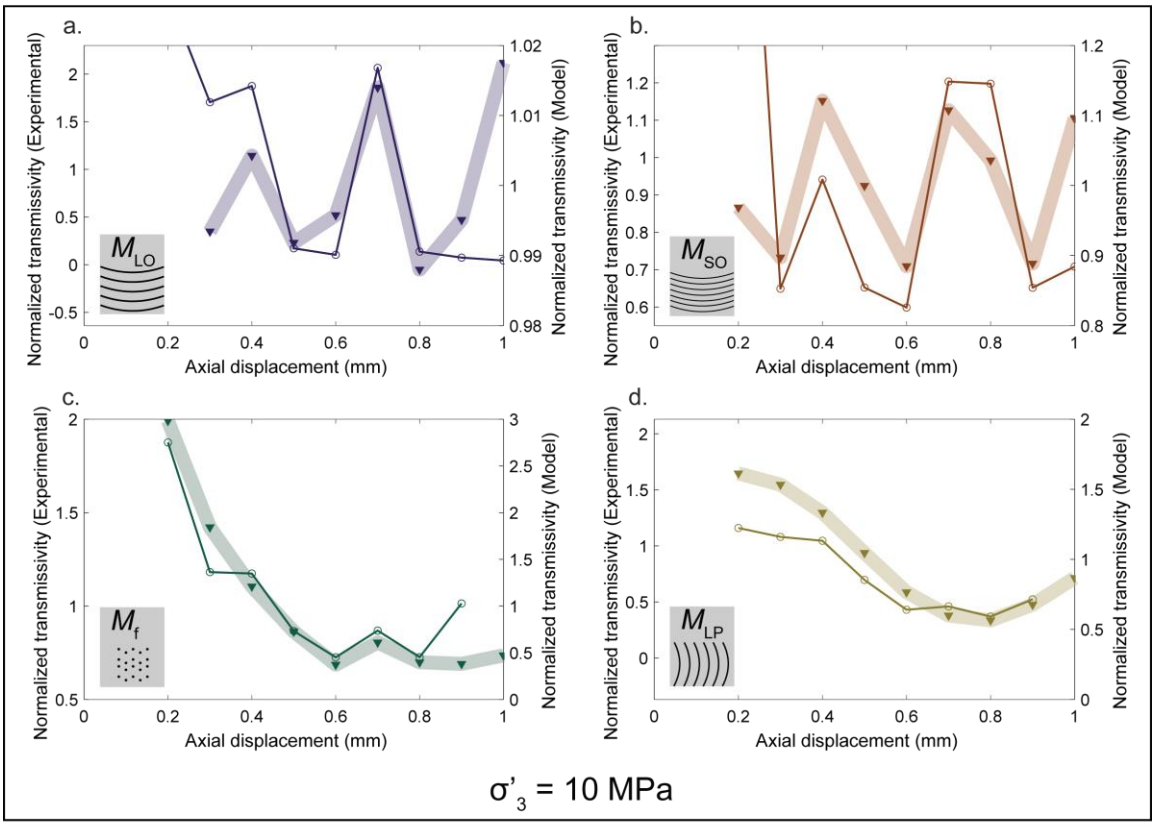
a.
b.
c.
d.
Normalized transmissivity (Experimental)
Normalized transmissivity (Model)
Axial displacement (mm)
M_{LO}
M_{SO}
M_f
M_{LP}
σ'$_3$ = 10 MPa

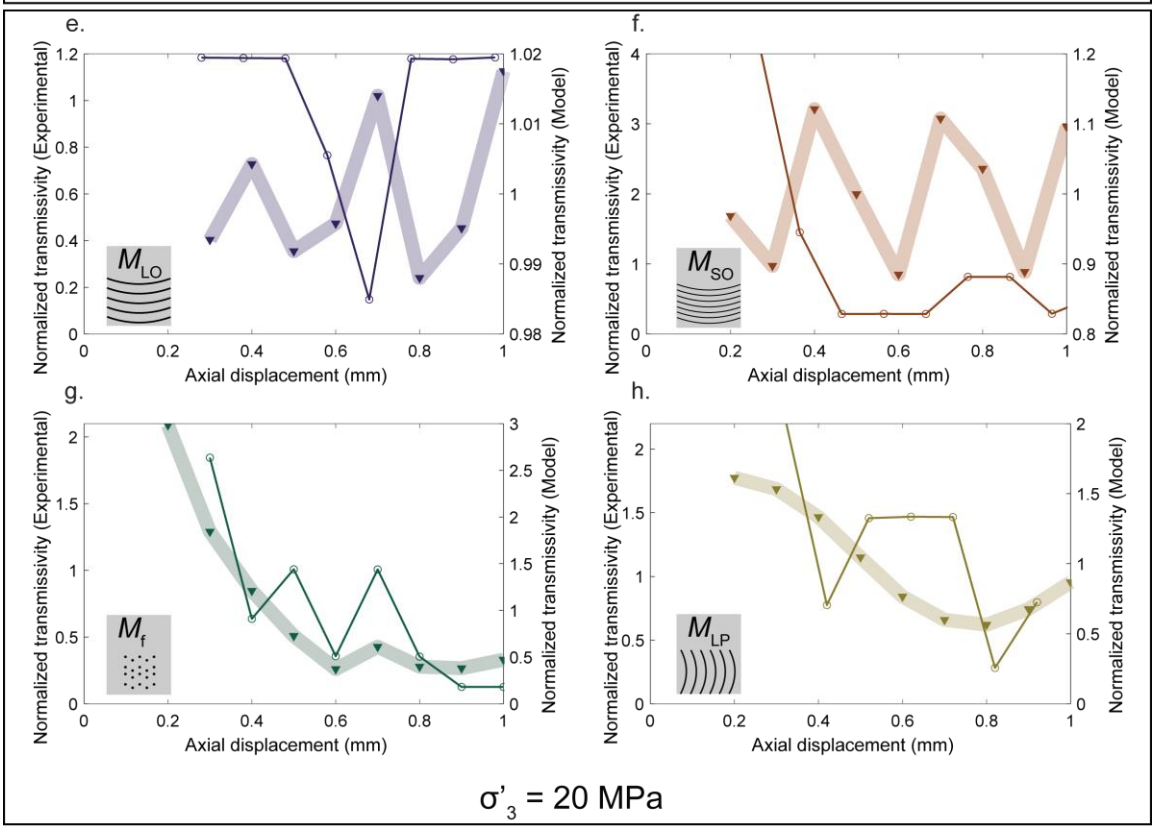
e.
f.
g.
h.
Normalized transmissivity (Experimental)
Normalized transmissivity (Model)
Axial displacement (mm)
M_{LO}
M_{SO}
M_f
M_{LP}
σ'$_3$ = 20 MPa

788

Figure 14. Transmissivity change during irreversible shear displacement. All transmissivity values are normalized by the mean transmissivity during shear to show the change with increasing displacement. Empty circles (full lines) represent experimental results and full triangles (transparent lines) represent numerical results described in section 6.2. a-d. Experiments at 10 MPa effective stress the simplified model captures the overall evolution of transmissivity with ongoing displacement. e-h. Experiments at 20 MPa effective stress. At high normal stress, the simplified model fails to capture the transmissivity change.

After shearing, the axial stress on all samples was decreased (i.e both normal and shear stress were decreased to isostatic loading conditions) and transmissivities measured again under isostatic stress conditions ($\sigma_1' = \sigma_3'$). The transmissivities after unloading (kt_{unl}) slightly increased with respect to the values measured at the end of the shearing stage (last points in Figure 6). Nevertheless, the transmissivity was far from being recovered to the isostatic initial transmissivity. The difference between kt_0 and kt_{unl} was usually more than an order of magnitude, meaning that after shearing, the faults hydraulic transport capacity was much smaller even if the stress state was the same. This result can be attributed to the production of wear products (thin gouge) which obstruct fluid flow in the fault, increasing the contact area and reducing the hydraulic aperture at given stress conditions (Faoro et al., 2009; Tanikawa et al., 2010; Rutter and Mecklenburgh, 2017, 2018). In our experiments, this is further supported by the evolution of surface roughness maps after shearing (Figure 8 and Figure 9). Similar observations have been made by Molecular Dynamics simulations of frictional sliding (Spijker et al., 2013) where roughness decreased exponentially during sliding in hard metals. In natural faults this effect is difficult to quantify. On the one hand, shear reactivation can decrease fault transmissivity due to the formation of wear products at small displacements. At large displacements, the wear products can become large enough that the transmissivity is in turn increased depending on fault roughness and rock properties (Molinari et al., 2018; Milanese et al., 2019). On the other hand, shear reactivation can increase transmissivity on ‘healed’ faults (e.g. if the fault’s core is composed of glassy products and or consolidated fault gouge), due to porosity unclogging (Elkhoury et al., 2011) or macroscopic dilatancy (Crawford et al., 2008; Faulkner et al., 2010; Cox, 2010; Zoback and Gorelick, 2012; Jeanne et al., 2018). It is possible that in faults with large scale roughness and heterogeneity, large displacements (larger than the

characteristic wavelength) lead to macroscopic dilation and increased fracture aperture (Chen et al., 2000; Watanabe et al., 2008; 2009; Ciardo and Lecampion, 2019).

Further experimental work dealing with the evolution of fault roughness is needed to understand how the production of wear products interacts with mechanical and hydraulic aperture changes.

6.3 Implications for geo-energy reservoirs

In our experiments, the fault's transmissivity first strongly decreased due to the application of normal stress, the sensitivity of fault's transmissivity to normal tress depended on fracture geometry (Figure 10, 14). When shear stress was applied, its influence was very small and was conditioned by the interaction between stress and fault geometries. Then, once faults were submitted to shear sliding (up to 1 mm), the transmissivity changes were small (often less than one order of magnitude) and its evolution could be predicted by the fault's geometry in experiments at low normal stress only. During the stimulation of deep geothermal reservoirs for example, one stimulation strategy to increase the production flow rate is to reactivate faults in shear, expecting that the shear displacement permanently increases transmissivity (Cladouhos et al., 2009; Breede et al., 2013). The strategy consists in injecting pressurized fluids into the fractured reservoir in order to decrease the effective normal stress on the fault, leading to reactivation. From the results in our study, we can observe that the reduction in normal stress can indeed increase the fault's transmissivity and that the magnitude of increase will depend on the fault surface geometry. If faults are flat but rough, the transmissivity increase will be smaller than if faults present some kind of macroscopic wavelength and heterogeneous topography (Watanabe et al., 2008; 2009 present somewhat similar observations in granitic rocks). In addition, decreasing the fault's effective normal stress will increase the shear-to-normal stress ratio (friction coefficient), thus transmissivity should change under the effect of shear stress, depending on the fault's geometry. This remains valid only if the overpressure in the reservoir is somehow maintained during the stimulation and production phases, reducing the reservoir's effective stress.

The usual idea regarding fault reactivation influence on transmissivity is that slip on rough faults generates an increase in hydraulic transport on the fault (Carey et al., 2015; Gale et al., 1990; Guo et al., 2013; Ishibashi et al., 2012; Lee and Cho, 2002; Yeo et al., 1998; Zambrano et al.,

2018; Pyrak-Nolte et al., 1987; Olsson and Brown, 1993; Esaki et al., 1999; Wenning et al., 2019). Nevertheless, in most of those studies, the shear displacements were in the range of 3 to 20 mm and/or on faults with large roughness (Chen et al., 2000; Wenning et al., 2019). Our results show that when shear slip occurred in the fault (<1 mm), transmissivity remained close to constant with very slight changes, in strong contrast to the usual understanding of shear reactivation described above. Very few other experimental studies have reported decrease in hydraulic transport properties with shear displacement (Rutter and Mecklenburgh, 2017; 2018; Faoro et al., 2009; Tankikawa et al., 2010). In deep geothermal reservoirs, stimulations that generate large shear displacements are usually associated with the occurrence of large magnitude seismic events. In the light of our results, inducing small shear displacements will not significantly increase the reservoir's fluid transport capacity. However, if the reservoir's fractures and faults are 'clogged' (due to the presence of frictional wear products or by mineral precipitation), it is highly possible that shear reactivation, followed by an unclogging treatment (chemical or hydraulic for example) does increase the fractures transmissivities (Elkhoury et al., 2011). This should be studied in future work.

We can conclude that changing the state of stress will improve fluid production in a larger scale than generating significant offsets in the fault (which can be technologically difficult). This can be done for example through stress preconditioning (Fryer et al., 2018; 2019).

A novelty from our study is the ability to 'predict' the shape of transmissivity changes with fault reactivation at low normal stress. Indeed, as shown in section 6.3 it seems that knowledge of fault surface geometry (even though this is a difficult measure to obtain) on faults submitted to small normal stresses can help estimate the shape of transmissivity change with shear displacement. Further work is nevertheless needed to estimate at which stress levels this prediction stops being accurate and to predict the change at high normal stress. Indeed, by preconditioning the reservoir (reducing the effective stress on it; Fryer et al., 2018; 2019), the predictions of transmissivity should become more accurate. We can speculate that the use of more complex models that include shear stress and wear processes can strongly improve the prediction of transmissivity with shear displacement (Aghababaei et al., 2017; Milanese et al., 2019; Molinari et al., 2018; Frerot et al., 2019; Yastrebov et al., 2017; Shvarts and Yastrebov, 2018a, ;2018b; Shvarts, 2019). The results obtained for a single rough-fault could then be input

into Discrete Fracture Models (DFM) to evaluate the hydraulic transport in fracture networks (McClure and Horne, 2013).

7 Conclusions

In this study, we developed an experimental technique to customize the surface roughness of real-rock samples which can be representative of engineered geothermal reservoirs (and more generally of underground carbonate reservoirs; Delle-Piane et al., 2015; DiPippo, 2012). The resulting surfaces had a fully controlled geometry which was precisely measured and analyzed using the Power Spectral Density of heights (Figures 1, 7, 8 and 9). Then, single fractures of Carrara marble with customized roughness were experimentally loaded under deep reservoir conditions (both under normal and shear loading) to study fluid flow through the wavy-rough fractures (Figures 5 and 6).

A numerical procedure was developed to simulate wavy-rough contacting surfaces (Section 3 and Figure 10b). It was validated with the experimental data, and it allowed for the isolation of the influence of different roughness parameters on fluid flow in fractures under normal loading. Under normal loading, the macroscopic geometry has a strong influence on the fracture's transmissivity decay (here fitted to an exponential decay) (Figure 10). Surfaces with grooves sub-orthogonal to fluid flow are more sensitive to the application of normal stress than samples with grooves sub-parallel to fluid flow and with no grooves in that order (Figure 10). A parametric analysis of the numerical procedure on samples with grooves sub-orthogonal to fluid flow showed that changes in the Hurst exponent and in the roll-off wavevector alone have little influence on transmissivity (Figure 11). On the other hand, the standard deviation of heights and the macroscopic wavelength have a strong influence on hydraulic transport capacity (Figure 11). The evolution of transmissivity has a strong non-monotonic dependence on these two parameters (Figure13).

Similar experimental fractures were loaded in shear and the numerical procedure was then used to isolate the effect of reversible shear loads on the fracture transmissivity (during elastic deformation, Figure 13). The influence of reversible shear load on fault's transmissivity is almost negligible and that its magnitude depends on the fault's geometry, thus it is not straightforward to estimate how reversible shear loading affects fracture transmissivity. Finally, the effect of irreversible shear displacement on transmissivity was studied with support on the

numerical procedure. It is found that increasing shear displacement (until 1 mm) generally decreases fracture transmissivity with slight variations at each displacement step (of 0.1 mm up to 1 mm; Figure 6). In that case, the transmissivity could be roughly predicted by changing the model geometry at low normal stress (Figure 13a-d) probably because wear was not too prominent. On the other hand, the geometrical model is completely off when normal stress is high during shear reactivation (Figure 13 e-h), probably due to prominent wear and surface topography changes (Figures 8, 9).

From this study, we observe that the main controls on fluid flow on rough fractures are in that order:1) stress applied on the fracture (normal to the fracture plane) 2) imbrication of the main wavelengths; 3) magnitude of the largest macroscopic wavelength; 4) RMS roughness; 5) shear reactivation; 6) Hurst exponent and roll-off wave-vector of the power spectral density of heights.

Further work is needed to develop a numerical procedure that allows simulating fractures under both normal and shear stresses. The target model should also include examination of shear induced plastic deformation and wear processes. This would allow coupling the evolution of fault roughness with the hydraulic transport properties as shear reactivation occurs.

In the light of our results, during EGS stimulations, small shear displacements will not significantly increase the reservoir's permeability (unless porosity unclogging occurs). In turn, reducing the effective stress on the reservoir's fractures and faults will generate large permeability increases and improve the ability to predict its evolution.

Acknowledgments and Data

M.A. and M.V. acknowledge the funding support from the Swiss National Science Foundation (SNF), project no. PYAPP2160588, and the technical staff at LEMR for help with sample preparation. M.V. acknowledges the European Research Council Starting Grant project 757290-BEFINE. M.A acknowledges Francois Passelègue; Federica Paglialunga, Carolina Giorgetti, and

Barnaby Fryer for fruitful discussions. The authors declare no competing interests. All the data related to this manuscript are being uploaded to Zenodo.org.

Annex 1: Deformation of intact Carrara Marble.

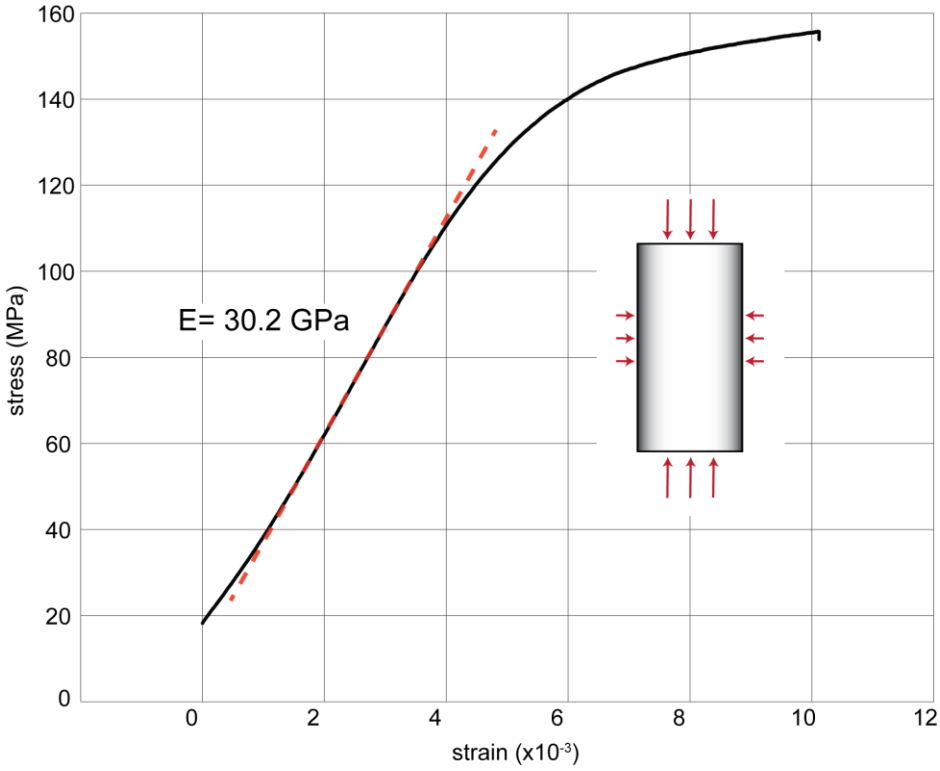

Figure A1. Experimental deformation of Carrara Marble. Differential stress versus axial strain. The data was used to determine the contact model parameters (E= 30 GPa).

Annex 2: Fluid flow model validation.

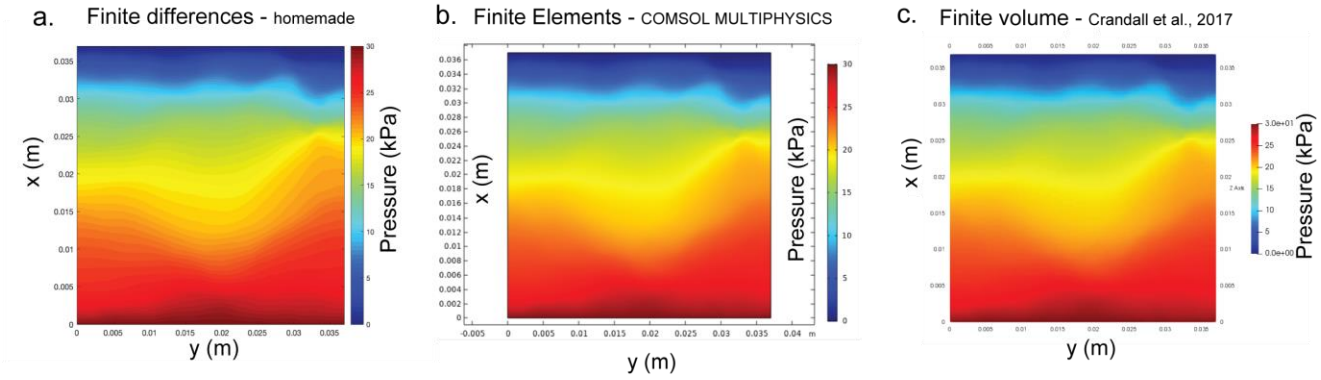

Figure A2. Fluid flow model validation. Pressure distribution obtained for the flow through parallel smooth plates. Three different models were tested for solving the Reynolds boundary lubrication approximation. a. Home-made finite difference model run on Matlab. b. Finite element model run on COMSOL multiphysics. c. Finite volume model

References

Acosta, M., Passelègue, F.X., Schubnel, A., Madariaga, R. and Violay, M., 2019. Can precursory moment release scale with earthquake magnitude? A view from the laboratory. *Geophysical Research Letters*, *46*(22), pp.12927-12937.

Acosta, M., Violay, M. 2020, Mechanical and hydraulic transport properties of transverse-isotropic Gneiss deformed under deep reservoir stress and pressure conditions. *International journal of rock mechanics and mining sciences*.

Aghababaei, R., Warner, D.H. and Molinari, J.F., 2016. Critical length scale controls adhesive wear mechanisms. *Nature communications*, *7*(1), pp.1-8.

Akchurin, A., Bosman, R., Lugt, P.M. and van Drogen, M., 2015. On a model for the prediction of the friction coefficient in mixed lubrication based on a load-sharing concept with measured surface roughness. *Tribology letters*, *59*(1), p.19.

Almakari, M., Chauris, H., Passelègue, F. X., Dublanchet, P., Gesret, A. 2020. Fault's hydraulic diffusivity enhancement during injection induced fault reactivation: Application of pore pressure diffusion inversions to laboratory injection experiments. *Submitted.*

Bay, N. and Wanheim, T., 1976. Real area of contact and friction stress at high pressure sliding contact. *Wear*, *38*(2), pp.201-209.

Bayart, E., Svetlizky, I. and Fineberg, J., 2016. Fracture mechanics determine the lengths of interface ruptures that mediate frictional motion. *Nature Physics*, *12*(2), pp.166-170.

Ben-David, O., Rubinstein, S.M. and Fineberg, J., 2010. Slip-stick and the evolution of frictional strength. *Nature*, *463*(7277), pp.76-79.

Bernabé, Y., Mok, U. and Evans, B., 2006. A note on the oscillating flow method for measuring rock permeability. *International journal of rock mechanics and mining sciences (1997)*, *43*(2), pp.311-316.

Breede, K., Dzebisashvili, K., Liu, X. and Falcone, G., 2013. A systematic review of enhanced (or engineered) geothermal systems: past, present and future. *Geothermal Energy*, *1*(1), p.4.

Brown, S., Caprihan, A. and Hardy, R., 1998. Experimental observation of fluid flow channels in a single fracture. *Journal of Geophysical Research: Solid Earth*, *103*(B3), pp.5125-5132.

Brown, S.R. and Scholz, C.H., 1985. Broad bandwidth study of the topography of natural rock surfaces. *Journal of Geophysical Research: Solid Earth*, *90*(B14), pp.12575-12582.

Brown, S.R., 1987. A note on the description of surface roughness using fractal dimension. *Geophysical Research Letters*, *14*(11), pp.1095-1098.

Brown, S.R., 1987. Fluid flow through rock joints: the effect of surface roughness. *Journal of Geophysical Research: Solid Earth*, *92*(B2), pp.1337-1347.

Brush, D.J. and Thomson, N.R., 2003. Fluid flow in synthetic rough-walled fractures: Navier-Stokes, Stokes, and local cubic law simulations. *Water Resources Research*, *39*(4).

Byerlee, J., 1978. Friction of rocks. In *Rock friction and earthquake prediction* (pp. 615-626). Birkhäuser, Basel.

Byerlee, J.D. and Summers, R., 1975. Stable sliding preceding stick-slip on fault surfaces in granite at high pressure. In *Earthquake Prediction and Rock Mechanics* (pp. 63-68). Birkhäuser, Basel.

Candela, T., Renard, F., Bouchon, M., Brouste, A., Marsan, D., Schmittbuhl, J. and Voisin, C., 2009. Characterization of fault roughness at various scales: Implications of three-dimensional high resolution topography measurements. In *Mechanics, structure and evolution of fault zones* (pp. 1817-1851). Birkhäuser Basel.

Candela, T., Renard, F., Klinger, Y., Mair, K., Schmittbuhl, J. and Brodsky, E.E., 2012. Roughness of fault surfaces over nine decades of length scales. *Journal of Geophysical Research: Solid Earth*, *117*(B8).

Carey, J.W., Lei, Z., Rougier, E., Mori, H. and Viswanathan, H., 2015. Fracture-permeability behavior of shale. *Journal of unconventional oil and gas resources*, *11*, pp.27-43.

Chen, J., 1995. *Effects of deformation on compressibility and permeability of Carrara Marble* (Doctoral dissertation, Massachusetts Institute of Technology).

Chen, Z., Narayan, S.P., Yang, Z. and Rahman, S.S., 2000. An experimental investigation of hydraulic behaviour of fractures and joints in granitic rock. *International Journal of Rock Mechanics and Mining Sciences*, *37*(7), pp.1061-1071.

Ciardo, F. and Lecampion, B., 2019. Effect of dilatancy on the transition from aseismic to seismic slip due to fluid injection in a fault. *Journal of Geophysical Research: Solid Earth*, *124*(4), pp.3724-3743.

Cladouhos, T., Petty, S., Foulger, G., Julian, B. and Fehler, M., 2010. Injection induced seismicity and geothermal energy. *GRC Transactions*, *34*, pp.1213-1220.

Cox, S.F., 2010. The application of failure mode diagrams for exploring the roles of fluid pressure and stress states in controlling styles of fracture-controlled permeability enhancement in faults and shear zones. *Geofluids*, *10*(1-2), pp.217-233.

Crandall, D., Moore, J., Gill, M. and Stadelman, M., 2017. CT scanning and flow measurements of shale fractures after multiple shearing events. *International Journal of Rock Mechanics and Mining Sciences*, *100*, pp.177-187.

Crawford, B.R., Faulkner, D.R. and Rutter, E.H., 2008. Strength, porosity, and permeability development during hydrostatic and shear loading of synthetic quartz-clay fault gouge. *Journal of Geophysical Research: Solid Earth*, *113*(B3).

Delle Piane, C., Arena, A., Sarout, J., Esteban, L. and Cazes, E., 2015. Micro-crack enhanced permeability in tight rocks: An experimental and microstructural study. *Tectonophysics*, *665*, pp.149-156.

Dieterich, J.H. and Kilgore, B.D., 1994. Direct observation of frictional contacts: New insights for state-dependent properties. *Pure and Applied Geophysics*, *143*(1-3), pp.283-302.

Dieterich, J.H., 1979. Modeling of rock friction: 1. Experimental results and constitutive equations. *Journal of Geophysical Research: Solid Earth*, *84*(B5), pp.2161-2168.

DiPippo, R., 2012. *Geothermal power plants: principles, applications, case studies and environmental impact*. Butterworth-Heinemann.

Edmond, J. M., and M. S. Paterson. "Volume changes during the deformation of rocks at high pressures." In *International Journal of Rock Mechanics and Mining Sciences and Geomechanics Abstracts*, vol. 9, no. 2, pp. 161-182. Pergamon, 1972.

Elkhoury, J.E., Niemeijer, A., Brodsky, E.E. and Marone, C., 2011. Laboratory observations of permeability enhancement by fluid pressure oscillation of in situ fractured rock. *Journal of Geophysical Research: Solid Earth*, *116*(B2).

Ellsworth, W.L., 2013. Injection-induced earthquakes. *Science*, *341*(6142), p.1225942.

Esaki, T., Du, S., Mitani, Y., Ikusada, K. and Jing, L., 1999. Development of a shear-flow test apparatus and determination of coupled properties for a single rock joint. *International Journal of Rock Mechanics and Mining Sciences*, *36*(5), pp.641-650.

Faoro, I., Niemeijer, A., Marone, C. and Elsworth, D., 2009. Influence of shear and deviatoric stress on the evolution of permeability in fractured rock. *Journal of Geophysical Research: Solid Earth*, *114*(B1).

Faulkner, D.R., Jackson, C.A.L., Lunn, R.J., Schlische, R.W., Shipton, Z.K., Wibberley, C.A.J. and Withjack, M.O., 2010. A review of recent developments concerning the structure, mechanics and fluid flow properties of fault zones. *Journal of Structural Geology*, *32*(11), pp.1557-1575.

Frérot, L., Bonnet, M., Molinari, J.F. and Anciaux, G., 2019. A Fourier-accelerated volume integral method for elastoplastic contact. *Computer Methods in Applied Mechanics and Engineering*, *351*, pp.951-976.

Fryer, B., Siddiqi, G. and Laloui, L., 2018. Reservoir Stimulation's Effect on Depletion-Induced Seismicity. *Journal of Geophysical Research: Solid Earth*, *123*(9), pp.7806-7823.

Fryer, B., Siddiqi, G. and Laloui, L., 2020. Injection-induced seismicity: strategies for reducing risk using high stress path reservoirs and temperature-induced stress preconditioning. *Geophysical Journal International*, *220*(2), pp.1436-1446.

Goebel, T.H. and Brodsky, E.E., 2018. The spatial footprint of injection wells in a global compilation of induced earthquake sequences. *Science*, *361*(6405), pp.899-904.

Grasselli, G. and Egger, P., 2003. Constitutive law for the shear strength of rock joints based on three-dimensional surface parameters. *International Journal of Rock Mechanics and Mining Sciences*, *40*(1), pp.25-40.

Grigoli, F., Cesca, S., Priolo, E., Rinaldi, A.P., Clinton, J.F., Stabile, T.A., Dost, B., Fernandez, M.G., Wiemer, S. and Dahm, T., 2017. Current challenges in monitoring, discrimination, and management of induced seismicity related to underground industrial activities: A European perspective. *Reviews of Geophysics*, *55*(2), pp.310-340.

Guo, T., Zhang, S., Gao, J., Zhang, J. and Yu, H., 2013. Experimental study of fracture permeability for stimulated reservoir volume (SRV) in shale formation. *Transport in porous media*, *98*(3), pp.525-542.

Hakami, E., 1989. *Water flow in single rock joints* (No. STRIPA-TR--89-08). Swedish Nuclear Fuel and Waste Management Co..

Ishibashi, T., Watanabe, N., Hirano, N., Okamoto, A. and Tsuchiya, N., 2012. Upgrading of aperture model based on surface geometry of natural fracture for evaluating channeling flow. *Geothermal Resources Council, Transactions*, *36*, pp.481-486.

Iwai, K., 1976. Fundamental studies of fluid flow through a single fracture. *Ph. D. thesis, Univ. of California*.

Jacobs, T.D., Junge, T. and Pastewka, L., 2017. Quantitative characterization of surface topography using spectral analysis. *Surface Topography: Metrology and Properties*, *5*(1), p.013001.

Jaeger, J.C., Cook, N.G. and Zimmerman, R., 2009. *Fundamentals of rock mechanics*. John Wiley and Sons.

Jeanne, P., Guglielmi, Y., Rutqvist, J., Nussbaum, C. and Birkholzer, J., 2018. Permeability variations associated with fault reactivation in a claystone formation investigated by field experiments and numerical simulations. *Journal of Geophysical Research: Solid Earth*, *123*(2), pp.1694-1710.

Kanafi, M., M., 2019. Radially averaged surface roughness/topography power spectrum (PSD) (https://www.mathworks.com/matlabcentral/fileexchange/54297-radially-averaged-surface-roughness-topography-power-spectrum-psd), MATLAB Central File Exchange. Retrieved February 23, 2019.

Kim, K.H., Ree, J.H., Kim, Y., Kim, S., Kang, S.Y. and Seo, W., 2018. Assessing whether the 2017 Mw 5.4 Pohang earthquake in South Korea was an induced event. *Science*, *360*(6392), pp.1007-1009.

Konzuk, J.S. and Kueper, B.H., 2004. Evaluation of cubic law based models describing single-phase flow through a rough-walled fracture. *Water Resources Research*, *40*(2).

Lee, H.S. and Cho, T.F., 2002. Hydraulic characteristics of rough fractures in linear flow under normal and shear load. *Rock Mechanics and Rock Engineering*, *35*(4), pp.299-318.

Lengliné, O., Lamourette, L., Vivin, L., Cuenot, N. and Schmittbuhl, J., 2014. Fluid-induced earthquakes with variable stress drop. *Journal of Geophysical Research: Solid Earth*, *119*(12), pp.8900-8913.

Lomize, G.M., 1951. Flow in fractured rocks. *Gosenergoizdat, Moscow*, *127*, p.197.

Lubrecht, A.A. and Ioannides, E., 1991. A fast solution of the dry contact problem and the associated sub-surface stress field, using multilevel techniques.

M., M., Kanafi (2018). Surface generator: artificial randomly rough surfaces (https://www.mathworks.com/matlabcentral/fileexchange/60817-surface-generator-artificial-randomly-rough-surfaces), MATLAB Central File Exchange. Retrieved February 23, 2018.

Means, W.D., 1987. A newly recognized type of slickenside striation. *Journal of Structural geology*, *9*(5-6), pp.585-590.

Milanese, E., Brink, T., Aghababaei, R. and Molinari, J.F., 2019. Emergence of self-affine surfaces during adhesive wear. *Nature communications*, *10*(1), pp.1-9.

Molinari, J.F., Aghababaei, R., Brink, T., Frérot, L. and Milanese, E., 2018. Adhesive wear mechanisms uncovered by atomistic simulations. *Friction*, *6*(3), pp.245-259.

Noël, C., Pimienta, L. and Violay, M., 2019. Time-dependent deformations of sandstone during pore fluid pressure oscillations: Implications for natural and induced seismicity. *Journal of Geophysical Research: Solid Earth*, *124*(1), pp.801-821.

Ohnaka, M., 2013. *The physics of rock failure and earthquakes*. Cambridge University Press.

Olsson, W.A. and Brown, S.R., 1993, December. Hydromechanical response of a fracture undergoing compression and shear. In *International journal of rock mechanics and mining sciences and geomechanics abstracts* (Vol. 30, No. 7, pp. 845-851). Pergamon.

Oron, A.P. and Berkowitz, B., 1998. Flow in rock fractures: The local cubic law assumption reexamined. *Water Resources Research*, *34*(11), pp.2811-2825.

Park, J.W. and Song, J.J., 2013. Numerical method for the determination of contact areas of a rock joint under normal and shear loads. *International Journal of Rock Mechanics and Mining Sciences*, *58*, pp.8-22.

Passelègue, F. X., Almakari, M., Dublanchet, P., Barras, F., Violay, M. 2020. On the nature of Earthquakes: from the field to the lab. *Submitted.*

Paterson, M.S. and Wong, T.F., 2005. *Experimental rock deformation-the brittle field*. Springer Science and Business Media.

Patir, N. and Cheng, H.S., 1978. An average flow model for determining effects of three-dimensional roughness on partial hydrodynamic lubrication.

Petit, J.P., 1987. Criteria for the sense of movement on fault surfaces in brittle rocks. *Journal of structural Geology*, *9*(5-6), pp.597-608.

Pieri, M., Burlini, L., Kunze, K., Stretton, I. and Olgaard, D.L., 2001. Rheological and microstructural evolution of Carrara Marble with high shear strain: results from high temperature torsion experiments. *Journal of Structural Geology*, *23*(9), pp.1393-1413.

Piggott, A.R. and Elsworth, D., 1992. Analytical models for flow through obstructed domains. *Journal of Geophysical Research: Solid Earth*, *97*(B2), pp.2085-2093.

Pingel, T.J., Clarke, K.C. and McBride, W.A., 2013. An improved simple morphological filter for the terrain classification of airborne LIDAR data. *ISPRS Journal of Photogrammetry and Remote Sensing*, *77*, pp.21-30.

Polonsky, I.A. and Keer, L.M., 1999. A numerical method for solving rough contact problems based on the multi-level multi-summation and conjugate gradient techniques. *Wear*, *231*(2), pp.206-219.

Power, W.L., Tullis, T.E., Brown, S.R., Boitnott, G.N. and Scholz, C.H., 1987. Roughness of natural fault surfaces. *Geophysical Research Letters*, *14*(1), pp.29-32.

Power, W.L. and Tullis, T.E., 1989. The relationship between slickenside surfaces in fine-grained quartz and the seismic cycle. *Journal of Structural Geology*, *11*(7), pp.879-893.

Pyrak-Nolte, L.J. and Morris, J.P., 2000. Single fractures under normal stress: The relation between fracture specific stiffness and fluid flow. *International Journal of Rock Mechanics and Mining Sciences*, *37*(1-2), pp.245-262.

Pyrak-Nolte, L.J., Cook, N.G. and Nolte, D.D., 1988. Fluid percolation through single fractures. *Geophysical Research Letters*, *15*(11), pp.1247-1250.

Renard, F., Candela, T. and Bouchaud, E., 2013. Constant dimensionality of fault roughness from the scale of micro-fractures to the scale of continents. *Geophysical Research Letters*, *40*(1), pp.83-87.

Renshaw, C.E., 1995. On the relationship between mechanical and hydraulic apertures in rough-walled fractures. *Journal of Geophysical Research: Solid Earth*, *100*(B12), pp.24629-24636.

Reynolds, Osborne. "IV. On the theory of lubrication and its application to Mr. Beauchamp tower's experiments, including an experimental determination of the viscosity of olive oil." *Philosophical transactions of the Royal Society of London* 177 (1886): 157-234.

Rutter, E.H. and Mecklenburgh, J., 2017. Hydraulic conductivity of bedding-parallel cracks in shale as a function of shear and normal stress. *Geological Society, London, Special Publications*, *454*(1), pp.67-84.

Rutter, E.H. and Mecklenburgh, J., 2018. Influence of normal and shear stress on the hydraulic transmissivity of thin cracks in a tight quartz sandstone, a granite, and a shale. *Journal of Geophysical Research: Solid Earth*, *123*(2), pp.1262-1285.

Sahli, R., Pallares, G., Ducottet, C., Ali, I.B., Al Akhrass, S., Guibert, M. and Scheibert, J., 2018. Evolution of real contact area under shear and the value of static friction of soft materials. *Proceedings of the National Academy of Sciences*, *115*(3), pp.471-476.

Scholz, C., Molnar, P. and Johnson, T., 1972. Detailed studies of frictional sliding of granite and implications for the earthquake mechanism. *Journal of geophysical research*, *77*(32), pp.6392-6406.

Shvarts, A., 2019. *Coupling mechanical frictional contact with interfacial fluid flow at small and large scales* (Doctoral dissertation).

Shvarts, A.G. and Yastrebov, V.A., 2018a. Trapped fluid in contact interface. *Journal of the Mechanics and Physics of Solids*, *119*, pp.140-162.

Shvarts, A.G. and Yastrebov, V.A., 2018b. Fluid flow across a wavy channel brought in contact. *Tribology International*, *126*, pp.116-126.

Sibson, R.H., 1994. Crustal stress, faulting and fluid flow. *Geological Society, London, Special Publications*, *78*(1), pp.69-84.

Sibson, R.H., 1996. Structural permeability of fluid-driven fault-fracture meshes. *Journal of Structural Geology*, *18*(8), pp.1031-1042.

Spijker, P., Anciaux, G. and Molinari, J.F., 2013. Relations between roughness, temperature and dry sliding friction at the atomic scale. *Tribology International*, *59*, pp.222-229.

Svetlizky, I. and Fineberg, J., 2014. Classical shear cracks drive the onset of dry frictional motion. *Nature*, *509*(7499), pp.205-208.

Tanikawa, W., Sakaguchi, M., Tadai, O. and Hirose, T., 2010. Influence of fault slip rate on shear-induced permeability. *Journal of Geophysical Research: Solid Earth*, *115*(B7).

Tembe, S., Lockner, D.A. and Wong, T.F., 2010. Effect of clay content and mineralogy on frictional sliding behavior of simulated gouges: Binary and ternary mixtures of quartz, illite, and montmorillonite. *Journal of Geophysical Research: Solid Earth*, *115*(B3).

Townend, J. and Zoback, M.D., 2000. How faulting keeps the crust strong. *Geology*, *28*(5), pp.399-402.

Toy, V.G., Niemeijer, A., Renard, F., Morales, L. and Wirth, R., 2017. Striation and slickenline development on quartz fault surfaces at crustal conditions: Origin and effect on friction. *Journal of Geophysical Research: Solid Earth*, *122*(5), pp.3497-3512.

Violay, M., Nielsen, S., Gibert, B., Spagnuolo, E., Cavallo, A., Azais, P., Vinciguerra, S. and Di Toro, G., 2014. Effect of water on the frictional behavior of cohesive rocks during earthquakes. *Geology*, *42*(1), pp.27-30.

Violay, M., Gibert, B., Mainprice, D. and Burg, J.P., 2015. Brittle versus ductile deformation as the main control of the deep fluid circulation in oceanic crust. *Geophysical Research Letters*, *42*(8), pp.2767-2773.

Violay, M., Heap, M.J., Acosta, M. and Madonna, C., 2017. Porosity evolution at the brittle-ductile transition in the continental crust: Implications for deep hydro-geothermal circulation. *Scientific reports*, *7*(1), pp.1-10.

Walsh, J.B. and Brace, W.F., 1984. The effect of pressure on porosity and the transport properties of rock. *Journal of Geophysical Research: Solid Earth*, *89*(B11), pp.9425-9431.

Walsh, J.B., 1981, Effect of pore pressure and confining pressure on fracture permeability. In *International Journal of Rock Mechanics and Mining Sciences and Geomechanics Abstracts* (Vol. 18, No. 5, pp. 429-435). Pergamon.

Watanabe, N., Hirano, N. and Tsuchiya, N., 2008. Determination of aperture structure and fluid flow in a rock fracture by high-resolution numerical modeling on the basis of a flow-through experiment under confining pressure. *Water Resources Research*, *44*(6).

Watanabe, N., Hirano, N. and Tsuchiya, N., 2009. Diversity of channeling flow in heterogeneous aperture distribution inferred from integrated experimental-numerical analysis on flow through shear fracture in granite. *Journal of Geophysical Research: Solid Earth*, *114*(B4).

Weber, B., Suhina, T., Brouwer, A.M. and Bonn, D., 2019. Frictional weakening of slip interfaces. *Science advances*, *5*(4), p.eaav7603.

Wenning, Q.C., Madonna, C., Kurotori, T. and Pini, R., 2019. Spatial mapping of fracture aperture changes with shear displacement using X-ray computerized tomography.

Witherspoon, P.A., Wang, J.S., Iwai, K. and Gale, J.E., 1980. Validity of cubic law for fluid flow in a deformable rock fracture. *Water resources research*, *16*(6), pp.1016-1024.

Yastrebov, V.A., Anciaux, G. and Molinari, J.F., 2017. The role of the roughness spectral breadth in elastic contact of rough surfaces. *Journal of the Mechanics and Physics of Solids*, *107*, pp.469-493.

Yeck, W.L., Weingarten, M., Benz, H.M., McNamara, D.E., Bergman, E.A., Herrmann, R.B., Rubinstein, J.L. and Earle, P.S., 2016. Far-field pressurization likely caused one of the largest injection induced earthquakes by reactivating a large preexisting basement fault structure. *Geophysical Research Letters*, *43*(19), pp.10-198.

Yeo, I.W., De Freitas, M.H. and Zimmerman, R.W., 1998. Effect of shear displacement on the aperture and permeability of a rock fracture. *International Journal of Rock Mechanics and Mining Sciences*, *35*(8), pp.1051-1070.

Zambrano, M., Tondi, E., Mancini, L., Lanzafame, G., Trias, F.X., Arzilli, F., Materazzi, M. and Torrieri, S., 2018. Fluid flow simulation and permeability computation in deformed porous carbonate grainstones. *Advances in water resources*, *115*, pp.95-111.

Zbinden, D., Rinaldi, A.P., Diehl, T. and Wiemer, S., 2019. Potential influence of overpressurized gas on the induced seismicity in the St. Gallen deep geothermal project (Switzerland): Gallen deep geothermal project (Switzerland). *Solid Earth Discussions*.

Zhang, S., Cox, S.F. and Paterson, M.S., 1994. The influence of room temperature deformation on porosity and permeability in calcite aggregates. *Journal of Geophysical Research: Solid Earth*, *99*(B8), pp.15761-15775.

Zimmerman, R.W. and Bodvarsson, G.S., 1996. Hydraulic conductivity of rock fractures. *Transport in porous media*, *23*(1), pp.1-30.

Zoback, Mark D., and Steven M. Gorelick. "Earthquake triggering and large-scale geologic storage of carbon dioxide." *Proceedings of the National Academy of Sciences* 109, no. 26 (2012): 10164-10168.